SANDIA REPORT
SAND20XX-XXXX
Printed September 2024

Sandia National Laboratories

A Bottom-Up Approach to Rational Design of Crystalline Materials: Investigation of Vibronic Coherences Underlying Exciton Dynamics in Semiconductors

Laura M. McCaslin, Krupa Ramasesha, Vitalie Stavila, Mark Allendorf, Ali Abou Taka, Mohana Shivanna, Joseph E. Reynolds III, Savini Bandaranayake, Neil Cole-Filipiak, Paul Schrader

Prepared by
Sandia National Laboratories
Albuquerque, New Mexico
87185 and Livermore,
California 94550

Issued by Sandia National Laboratories, operated for the United States Department of Energy by National Technology & Engineering Solutions of Sandia, LLC.

Available to DOE and DOE contractors from
U.S. Department of Energy
Office of Scientific and Technical Information
P.O. Box 62
Oak Ridge, TN 37831

Telephone: (865) 576-8401
Facsimile: (865) 576-5728
E-Mail: reports@osti.gov
Online ordering: http://www.osti.gov/scitech

Available to the public from
U.S. Department of Commerce
National Technical Information Service
5301 Shawnee Rd
Alexandria, VA 22312

Telephone: (800) 553-6847
Facsimile: (703) 605-6900
E-Mail: orders@ntis.gov
Online order: https://classic.ntis.gov/help/order-methods/

ABSTRACT

In this project we uncovered structure-function relationships of donor-acceptor co-crystals used to develop next-generation optoelectronic devices. Unraveling the photodynamics of molecular crystalline materials poses many challenges for spectroscopy due to broad, overlapping features representing numerous underlying dynamical processes. This leads researchers to make many assumptions about the dynamics of a system in choosing an appropriate kinetic fitting model. Computationally, electronic structure methods are either prohibitively expensive or underdeveloped for computing the excited state structure of molecular materials, especially states that exhibit charge transfer. Researchers must therefore perform calculations of excited electronic states using truncated models of molecular materials. Here we present a joint experimental-theoretical approach to bridging the gap between the photodynamics of a molecular material and its constituent molecules. We focus our efforts on quantifying the timescales and mechanisms of photoexcitation in donor-acceptor co-crystals and donor-acceptor dimers where the lowest-lying excited state is characterized by charge transfer from the donor to the acceptor. We employ ultrafast UV pump, UV-Vis probe transient absorption spectroscopy to unravel the time-resolved spectroscopic signatures of the photodynamics in both the crystalline material and donor-acceptor dimers in solution. We perform electronic structure and excited state dynamics calculations of the dimers to inform kinetic fitting models and assign the spectral features. The photodynamics of the crystal vs. dimer systems have many similarities, enabling unprecedented insights into the formation and evolution of charge transfer excitons in the crystalline systems.

ACKNOWLEDGEMENTS

We would like to acknowledge Patrick Feng for his help to perform time-resolved photoluminescence measurements of the co-crystals. We also acknowledge Prof. John Herbert for his contributions to our understanding of computing the degree of charge transfer with time-dependent density functional theory. We thank the team of Prof. Marissa Weichman, including Ashley Fidlar, Alexander McKillop, and Liying Chen for performing transient absorption experiments of the PDI co-crystals.

CONTENTS

Abstract 3

Acknowledgements 4

Acronyms and Terms 9

1. Introduction 11

2. Methods 12
   - 2.1. Synthesis, Sample Preparation, and Characterization 12
     - 2.1.1. Synthesis and characterization of co-crystals 12
     - 2.1.2. Preparation of Npe:TCNB dimer solutions 17
     - 2.1.3. Confining and characterizing D-A pairs in MOFs 17
   - 2.2. UV pump, UV-Vis probe TAS and characterization 20
     - 2.2.1. TAS of Npe:TCNB co-crystals and dimers 20
     - 2.2.2. TAS of co-crystals with a PDI acceptor 22
   - 2.3. Computational Methods 22
     - 2.3.1. Npe:TCNB 22
     - 2.3.2. PDI Acceptors 23
     - 2.3.3. Assessing metrics for quantifying charge transfer 23

3. CT exciton dynamics of Npe:TCNB 24
   - 3.1. UV pump, UV-Vis probe ultrafast TAS 24
   - 3.2. Kinetic fitting of TAS data 24
     - 3.2.1. First-order decay model 25
     - 3.2.2. First- and second-order decay model 25
     - 3.2.3. Branched model 27
   - 3.3. Predicting TAS signatures using AIMD and electronic structure calculations 27

4. CT exciton dynamics of co-crystals with a PDI acceptor 30
   - 4.1. Static UV-Vis Absorption Spectra 30
   - 4.2. PDI:PXX 30
   - 4.3. PDI:perylene 34
   - 4.4. PDI:triphenylene 37

5. Assessing metrics for computing DCT 41
   - 5.1. Background 41
   - 5.2. Assessing the quality of CT metrics 41
     - 5.2.1. Dependence on density functional 41
     - 5.2.2. Dependence on basis set 43

6. Professional service 45

References 46

Distribution 51

LIST OF FIGURES

Figure 1: Chemical structure of different acceptor and donor molecules selected for this project. ... 13

Figure 2: Crystal structures of co-crystals a) PDI:PXX, b) PDI:perylene and c) PDI:triphenylene.... 14

Figure 3: Crystal structure of co-crystals a) Ph_4PDI:PXX, b) Ph_4PDI:perylene and c) Ph_4PDI:coronene. 14

Figure 4: Experimental PXRD measurements the PDI:donor and Ph_4PDI:donor co-crystals, compared with the calculated pattern obtained from the crystal structure. 15
Figure 5: TGA (a) and DSC (b) measurements for PDI and Ph_4PDI with different donor molecules. 16
Figure 6: UV-Vis diffuse reflectance spectra for individual monomers and dimers of different PDI:donor and Ph_4PDI:donor co-crystals. 16
Figure 7: Structural representations of co-crystals a) PDI:coronene, b) PDI:pyrene and c) Ph_4PDI:pyrene. 17
Figure 8: a) MOF-177+TCNQ:naphthalene, b) MOF-177+TCNQ, C) MOF-177+ naphthalene, and d) MOF-177. 18
Figure 9: ^{1}H NMR measurements to confirm the presence of D-A pairs, a) TCNQ:napthalene and b) TCNQ:pyrene. 19
Figure 10: UV-Vis diffuse reflectance spectra measured for MOF, monomers@MOF, and D-A@MOF. 20
Figure 11: SVD analysis of Npe:TCNB TAS data. a) SVD Component strength, b) Temporal development of SVD, c) Spectral components from SVD analysis. 21
Figure 12: Ultrafast UV pump, UV-Vis probe TAS of the Npe:TCNB co-crystal. Differential absorption (ΔmOD) is shown as a function of wavelength and time in ps. 24
Figure 13: Plots of the fitted (solid) and experimental (dots) data at 450, 500, and 580 nm with fits given by (a) the first-order decay model, (b) the first- + second-order order decay model, and (c) the branched model. 26
Figure 14: Simulated TAS of Npe:TCNB dimers in vacuum (top row) and 1,4-dioxane (bottom row) originating from the S_1, T_1, and S_0 states. 28
Figure 15: a) TAS of Npe:TCNB dimers in 1,4-dioxane, b) TAS lineouts of Npe monomer (orange) and Npe:TCNB dimer (blue) in 1,4-dioxane solvent at 1, 10, 100, and 1000 ps time delays. 29
Figure 16: Static UV-Vis absorption spectra of a) PDI:PXX b) PDI:perylene and c) PDI:triphenylene co-crystals (black lines) and the respective pump excitation wavelengths (colored lines). 30
Figure 17: False color map of the TAS of PDI:PXX co-crystals, showing the differential absorption as a function of time delay and wavelength. b) TAS lineouts at select time delays. 31
Figure 18: a) EADS corresponding to species A (blue), B (orange) and C (yellow). b) Kinetic traces at ~740 and ~752 nm from 1 to 7500 ps post-excitation. Circles represent experimental data, and solid lines represent fits obtained from global fitting. 32
Figure 19: Optimized geometries (1a–d) of PDI:PXX found with CAM-B3LYP-D3/6-31+G(d,p) and the experimental CIF structure. Energies (eV) are reported relative to the lowest-energy structure (1a) and include zero-point energy corrections. The calculated degree of CT is reported for S_0 and S_1, as well as the associated S_0–S_1 oscillator strengths. 32
Figure 20: a) The simulated absorption spectra of PDI:PXX conformers a-d. b) The simulated absorption spectra of the best candidate for PDI:PXX conformer. c) Diffuse reflectance spectra of PDI:PXX. 33
Figure 21: Simulated TAS of PDI:PXX dimers in vacuum originating from the S_0, S_1, and T_1 states. 33
Figure 22: a) False color map of the TAS of PDI:perylene co-crystals, showing the differential absorption as a function of wavelength and time. The white area depicts the region of the spectrum that contains scatter from the pump pulse and hence cannot be interpreted. b) TAS lineouts at select time delays. 34

Figure 23: a) Evolution associated difference spectra corresponding to species A (blue), B (orange) and C (yellow). b) Kinetic traces at ~494 (green), ~510 (purple) and ~750 (pink) nm from 1 to 7500 ps post-excitation. Circles represent experimental data and solid lines represent fits obtained from global fitting. 35
Figure 24: Optimized geometries (2a–c) of PDI:perylene computed with CAM-B3LYP-D3/6-31+G(d,p) compared to the experimental crystal structure. Energies (eV) are reported relative to the lowest-energy structure (2a) and include zero-point energy corrections. The calculated DCT is reported for S_0 and S_1, as well as the associated S_0–S_1 oscillator strengths. 35
Figure 25: a) The simulated absorption spectra of PDI:perylene conformers, b) The simulated absorption spectra of the best candidate for PDI:perylene conformer, c) Diffuse reflectance spectra of PDI:perylene. 36
Figure 26: Simulated TAS of PDI:PXX dimers in vacuum originating from the S_0, S_1, and T_1 states. 36
Figure 27: a) False color map of the TAS of the PDI:triphenylene co-crystal system, showing the differential absorption as a function of wavelength and time delay. b) Transient spectra at select time delays. 37
Figure 28: a) Evolution associated difference spectra corresponding to species A (blue), B (orange) and C (yellow). b) Kinetic traces at ~735 and 765 nm from 1 to 7500 ps, post excitation. Circles represent experimental data and solid lines represent fits obtained from global fitting. 38
Figure 29: a) Evolution associated difference spectra corresponding to species A (blue) and B (orange). b) Kinetic traces at ~735 (green) and ~765 (purple) nm from 1 to 7500 ps post-excitation. Circles represent experimental data and solid lines represent fits obtained from global fitting. 39
Figure 30: Optimized geometries (3a–c) of PDI:triphenylene computed with CAM-B3LYP-D3/6-31+G(d,p) and the experimental crystal structure. Energies (eV) are reported relative to the lowest-energy structure (3a) and include zero-point energy corrections. The calculated DCT is reported for S_0, S_1, and S_2 as well as their associated S_0–$S_{1\text{-}2}$ oscillator strengths. 39
Figure 31: a) Diffuse reflectance spectra of PDI:triphenylene. b) The simulated absorption spectra of the best candidate dimer (Conformer 3b). 40
Figure 32: Plots of orbital similarity, spatial overlap, orbital gap ratio, and E_{HOMO} - E_{LUMO} vs. S_1 DCT using the CAM-B3LYP-D, ωB97X-D, M062X, PBE1PBE-D, and APFD functionals and a 6-31G+(d,p) basis set. 42
Figure 33: Plots of orbital similarity, spatial overlap, orbital gap ratio, and E_{HOMO} – E_{LUMO} vs. S_1 DCT using the aggregated data across the five DFT functionals. 43
Figure 34: Plots of orbital similarity, spatial overlap, orbital gap ratio, and E_{HOMO} – E_{LUMO} vs. S_1 DCT using ωB97X-D with 6-31G, 6-31+G(d,p), and 6-311++G(3df,3pd) basis sets. 44

LIST OF TABLES

Table 1: k_1 and k_2 time constants obtained for different co-crystals by fitting a two-step sequential model 38

This page left blank

ACRONYMS AND TERMS

Acronym/Term	Definition
D-A	Donor-acceptor
CT	Charge transfer
SCXRD	Single crystal x-ray crystallography
FTIR	Fourier transform infrared
PXRD	Powder x-ray diffraction
PL	Photoluminescence
PDI	N,N'-Bis(3-pentyl)perylene-3,4,9,10-bis(dicarboximide)
Ph4PDI	N,N-Bis(3-pentyl)-2,5,8,11 tetraphenylperylene-3,4:9,10-bis(dicarboximide)
PXX	Peri-xanthenoxanthene
Npe	4-(1-Naphthylvinyl) pyridine
TCNB	1,2,4,5-Tetracyanobenzene
TCNQ	7,7,8,8-Tetracyanoquinodimethane
RT	Room temperature
TGA	Thermogravimetric analysis
DSC	Differential scanning calorimetry
MOF	Metal organic framework
DCM	Dichloromethane
SVD	Singular value decomposition
IRF	Instrument response function
FWHM	Full-width half maximum
DFT	Density functional theory
TDDFT	Time-dependent density functional theory
AIMD	Ab initio molecular dynamics
DCT	Degree of charge transfer
TDM	Transition density matrix
GSB	Ground state bleach
ISC	Intersystem crossing
EADS	Evolution assisted differential spectra
PES	Potential energy surface
HTS	High-throughput screening
XC	Exchange-correlation

This page left blank

1. INTRODUCTION

Organic donor-acceptor (D-A) co-crystals have emerged as an important class of materials in the field of optoelectronics due to their unique photophysical properties for applications in integrated photonics, photovoltaic devices, and organic light-emitting diodes.[1-5] The tunability of these properties, through choices of donor and acceptor, offers a promising avenue for the development of next-generation optoelectronic devices. D-A co-crystals are composed of electron-donor and acceptor molecules which self-assemble in solution due to strong non-covalent interactions between the components, yielding materials with desirable morphologies, sizes, and functional properties.

Upon excitation with UV-Vis radiation, D-A co-crystals form charge transfer (CT) excitons, which are characterized by electron transfer from the donor to the acceptor, forming a radical ion pair.[6-8] These CT excitons can relax through a variety of radiative and non-radiative mechanisms that include one or multiple excitons. One of the predominant techniques for unraveling the CT exciton dynamics and relaxation mechanisms is UV pump, UV-Vis probe ultrafast transient absorption spectroscopy (TAS), (see References [9-11] and citations within). A major challenge in these experiments is the analysis of the dynamical data, often done with kinetic fitting techniques. Due to the significant number of underlying dynamical mechanisms, many broad and overlapping features emerge in the TAS. This leads to multiple kinetic models that are both rational and provide adequate fits to the data.

In this project we present an integrated experimental-theoretical approach to overcoming some of the challenges in analyzing time-resolved spectroscopy of CT exciton dynamics in D-A co-crystals. First, we compare the UV pump, UV-Vis probe ultrafast TAS of the co-crystals with dimer solutions of the constituent molecules. Second, we perform high-level electronic structure and non-adiabatic dynamics calculations of the D-A dimers to construct a basis set for improved fits and assignment of the TAS data. Through these detailed studies we discover structure-property relationships and develop a novel metric for predicting CT exciton lifetimes in D-A co-crystals based on the degree of S_1 CT.

2. METHODS

2.1. Synthesis, Sample Preparation, and Characterization

2.1.1. Synthesis and characterization of co-crystals

The synthesis of D-A co-crystals consisting of molecules shown in Figure 1 was performed using known liquid-phase approaches using appropriate solvents.[12-14] Liquid-phase methods, such as slow evaporation, drop-casting, and diffusion, are commonly used to prepare organic co-crystals due to their low cost and ease of preparation. By varying solvent type, temperature, and concentration, different morphologies and sizes of co-crystals can be obtained. The slow evaporation method involves dissolving donor and acceptor precursors in a solvent and allowing it to evaporate, leading to crystallization. In drop-casting, a solution is placed on a substrate, and co-crystals form as the solvent evaporates. The liquid-phase methods are particularly useful for creating micro- and nanoscale co-crystals for optoelectronic devices, and in selected cases large enough crystals can be obtained for single-crystal X-ray crystallography.

2.1.1.1. General Instrumentation

Single Crystal X-Ray Crystallography (SCXRD): Suitable crystals were mounted on a thin glass fiber using perfluoropolyether oil, which was frozen in situ by a nitrogen gas cryostream flow. Data collection was performed on either on a Rigaku Super Nova diffractometer equipped with an AtlasS2 CCD, and Oxford 700 low-temperature attachment, using CuKα (λ = 1.54184), or using a Rigaku Synergy-S diffractometer equipped with dual-beam microfocus Cu and Mo radiation sources and paired with a Rigaku's HyPix. Using Olex2, structures were solved with the SHELX structure solution program using Direct Methods and refined with the SHELXL refinement package using Least Squares minimization.
Fourier transform infrared (FTIR): Spectra were obtained with an Agilent Cary-630 spectrometer, with an attenuated total reflectance module containing a diamond crystal in an argon glovebox.
Powder X-ray diffraction (PXRD): Patterns for the bulk powders were collected with a Panalytical Empyrean Diffractometer system equipped with a PIXcel3D detector using Cu Kα radiation using samples loaded in glass capillaries (Charles Supper, Inc.) and sealed with vacuum grease.
Raman: Spectra were obtained with a Metrohm USA i-Raman-Plus spectrometer with a 532 nm laser using an average of ten 10 second scans.
Elemental microanalyses: Performed by Galbraith Laboratories, Inc. (Knoxville, TN).
Photoluminescence (PL): Photoluminescence spectra were collected using an Edinburgh Instruments FLS1000 fluorimeter equipped with a 450 W xenon arc lamp for steady-state measurements and a 375 nm picosecond pulsed light emitting diodes for time-resolved measurements. Single-grating Czerny-Turner excitation and emission monochromators were used along with a cooled PMT-900 photomultiplier detector that covers a range of 185-900 nm. Absorption spectra were collected between 300 - 540 nm monitoring the wavelength of 550 nm. Emission spectra were collected between 424 - 740 nm with an excitation wavelength of 375 nm.
UV-Vis Diffuse Reflectance Spectroscopy: A commercial UV-visible spectrometer (Cary 3000) was used to collect all static UV-visible spectra

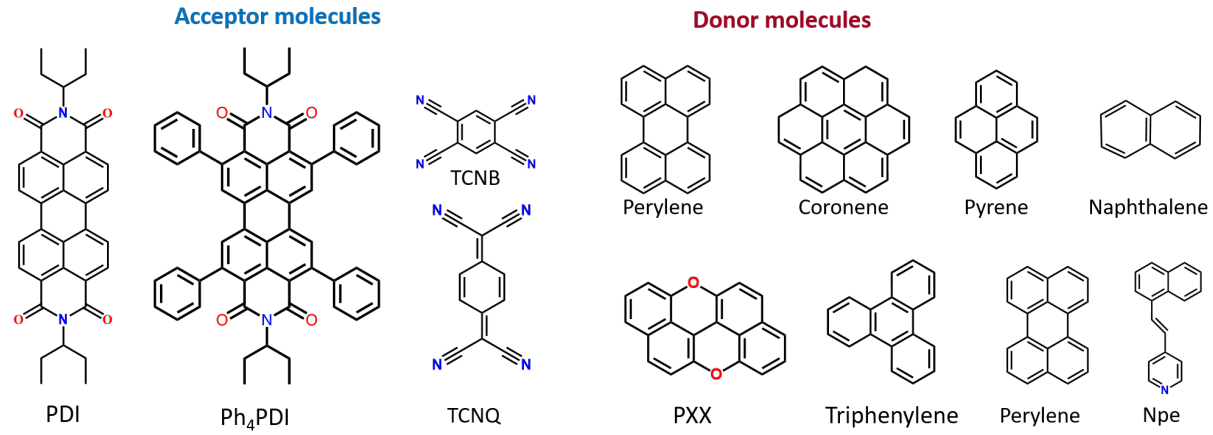

Figure 1: Chemical structure of different acceptor and donor molecules selected for this project.

2.1.1.2. Synthesis of PDI:PXX, PDI:perylene, PDI:triphenylene

PDI (5.3 mg, 0.01 mmol) and PXX (2.82 mg, 0.01 mmol) were dissolved in a chloroform/ethanol or chloroform/methanol mixture (2ml:1ml) in a 4 ml glass vial at RT. The vial was capped tightly and placed in an oven at 80°C for 10-15 minutes to obtain a clear solution. The glass vial was left at RT for slow evaporation, resulting in dark green/brown rod-shaped crystals within a day. Similarly, rod-shaped dark green single crystals of PDI:perylene were grown by slow evaporation of PDI (5.3 mg, 0.01 mmol) and perylene (2.52 mg, 0.01 mmol) using a toluene/ethanol or toluene/methanol mixture at RT. To obtain red color single crystals of PDI:triphenylene, both PDI (5.3 mg, 0.01mmol) and triphenylene (2.3 mg, 0.01 mmol) were dissolved in a chloroform/ethanol or chloroform/methanol mixture. Suitable single crystals were selected for SCXRD and data collection was achieved at 100 K. The analysis found that all three co-crystals PDI:PXX, PDI:perylene, and PDI:triphenylene crystallize in a triclinic system with the P-1 space group. The acceptor (PDI) and donor molecules are packed one above other through π-π stacking interaction with an interatomic distance of 3.494, 3.42 and 3.40 Å for PDI:PXX, PDI:perylene, and PDI:triphenylene, respectively, as shown in Figure 2.

2.1.1.3. Synthesis of Ph_4PDI:PXX, Ph_4PDI:perylene and Ph_4PDI:coronene

To vary the functionality of electron withdrawing moiety, we synthesized the aromatic derivative Ph_4PDI and combined it with donor molecules PXX, perylene, and coronene. This led to synthesis of Ph_4PDI:PXX, Ph_4PDI:perylene and Ph_4PDI:coronene co-crystals with a 1:1 ratio in single crystalline phases. The synthesis was achieved by mixing 1:1 ratios of donor and acceptor molecules in appropriate solvent mixtures and slowly evaporating at RT. Ph_4PDI (4.1 mg, 0.005 mmol) and PXX (1.4 mg, 0.005 mmol) were dissolved in a toluene/ethanol (3:1) mixture in a 4 ml glass vial and heated at 80°C for 20 mins. After solution became clear, the vial was kept at RT for 1-2 days to grow dark brown crystals. The same procedure was used to grow single crystals of Ph_4PDI:perylene (0.005 mmol each) and Ph_4PDI-coronene (0.005 mmol each), but in toluene/methanol in a 3:1 ratio.

The suitable single crystals were selected for SCXRD and the analysis found that the co-crystals Ph_4PDI:PXX, Ph_4PDI:perylene, and Ph_4PDI:coronene crystallize in Pnma, I2, and P21/n space groups, respectively. The co-crystals formed in 1:1 ratios, held with π-π stacking interactions with interatomic distances of 3.46, 3.476 and 3.61 Å for Ph_4PDI:PXX, Ph_4PDI:perylene, and Ph_4PDI:triphenylene, respectively (Figure 3).

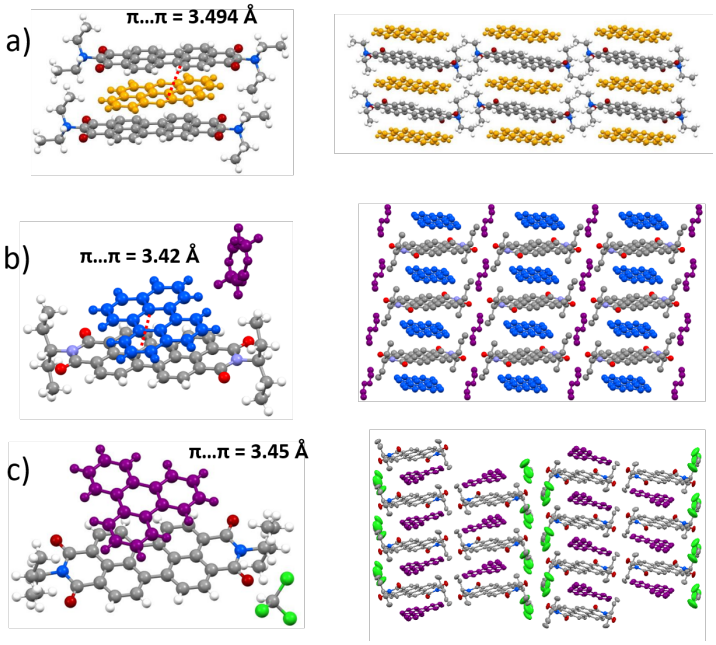

Figure 2: Crystal structures of co-crystals a) PDI:PXX, b) PDI:perylene and c) PDI:triphenylene.

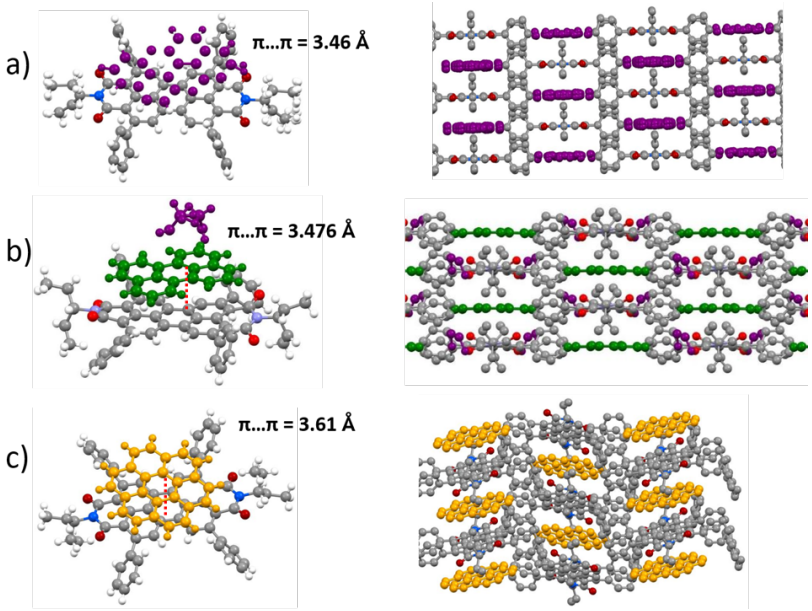

Figure 3: Crystal structure of co-crystals a) Ph_4PDI:PXX, b) Ph_4PDI:perylene and c) Ph_4PDI:coronene.

To verify the phase purity of as synthesized co-crystals, we carried out PXRD characterization. The synthesized crystals were ground into a powder, placed on a zero-background sample holder, mounted to a bracket flat sample stage, and exposed to x-ray radiation. These measurements revealed that the pattern of synthesized co-crystals matched with the calculated pattern obtained from the crystal structure, as shown in Figure 4. Thermogravimetric analysis (TGA) and differential scanning calorimetry (DSC) measurements were carried out under nitrogen using a TA Q50 instrument. Experiments were conducted using platinum pans with a flow rate of 60 mL min^{-1} of nitrogen gas. The TGA measurements indicated that the stability of synthesized co-crystals as shown in Figure 5a. The solvent weight loss found in the four co-crystals is in good agreement with the solvent found in the crystal structure lattice. In the case of PDI:PXX, no solvent was found in the crystal structure or TGA measurements. In thermal stability experiments, the as-synthesized co-crystals were found to be stable up to 300°C, except PDI:triphenylene, which is stable up to 250°C. DSC measurements are in good agreement with the TGA measurements in terms of solvent loss and decomposition of crystal structure, as shown in Figure 5b.

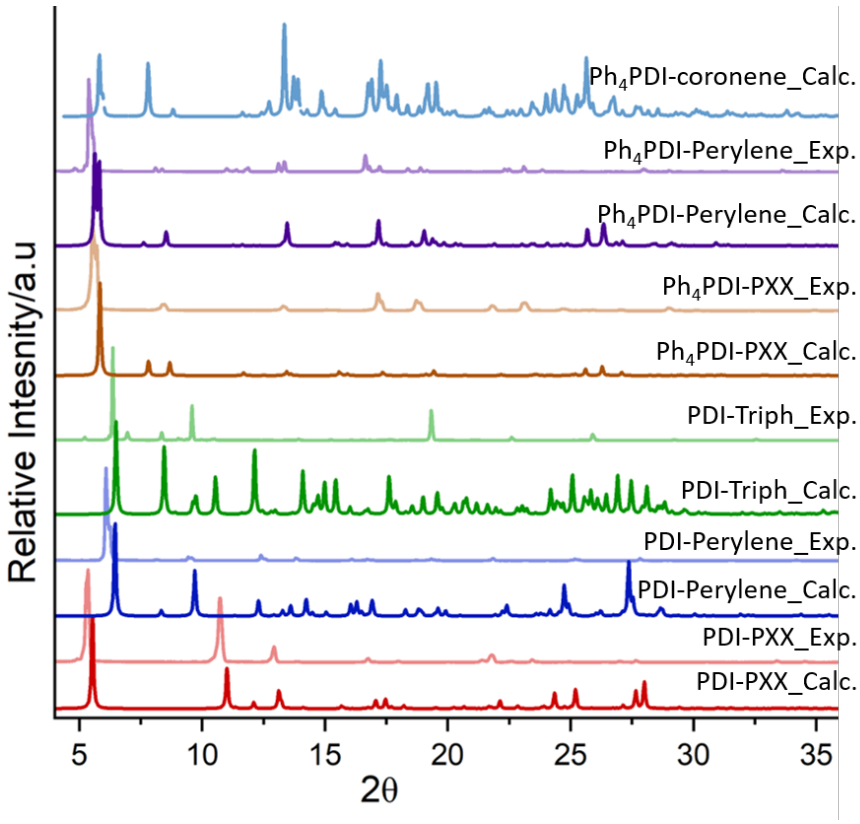

Figure 4: Experimental PXRD measurements the PDI:donor and Ph_4PDI:donor co-crystals, compared with the calculated pattern obtained from the crystal structure.

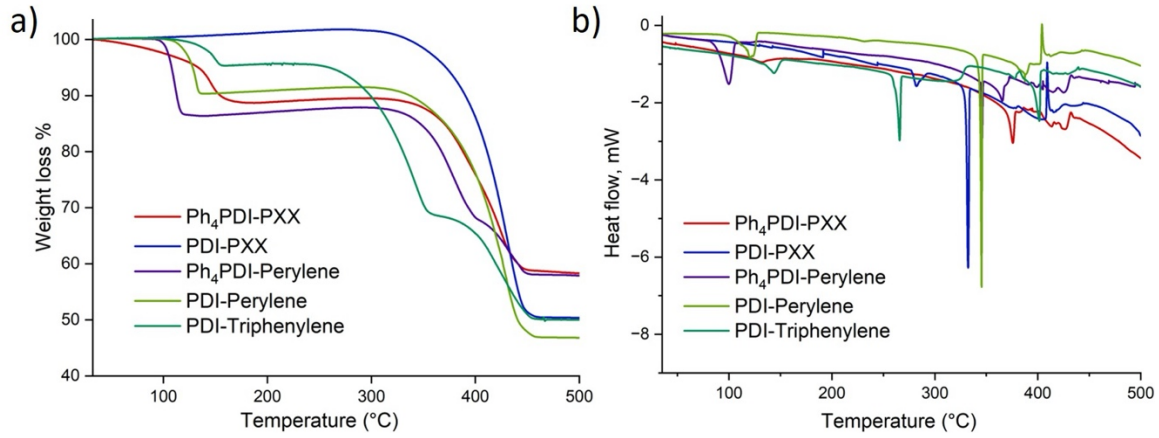

Figure 5: TGA (a) and DSC (b) measurements for PDI and Ph_4PDI with different donor molecules.

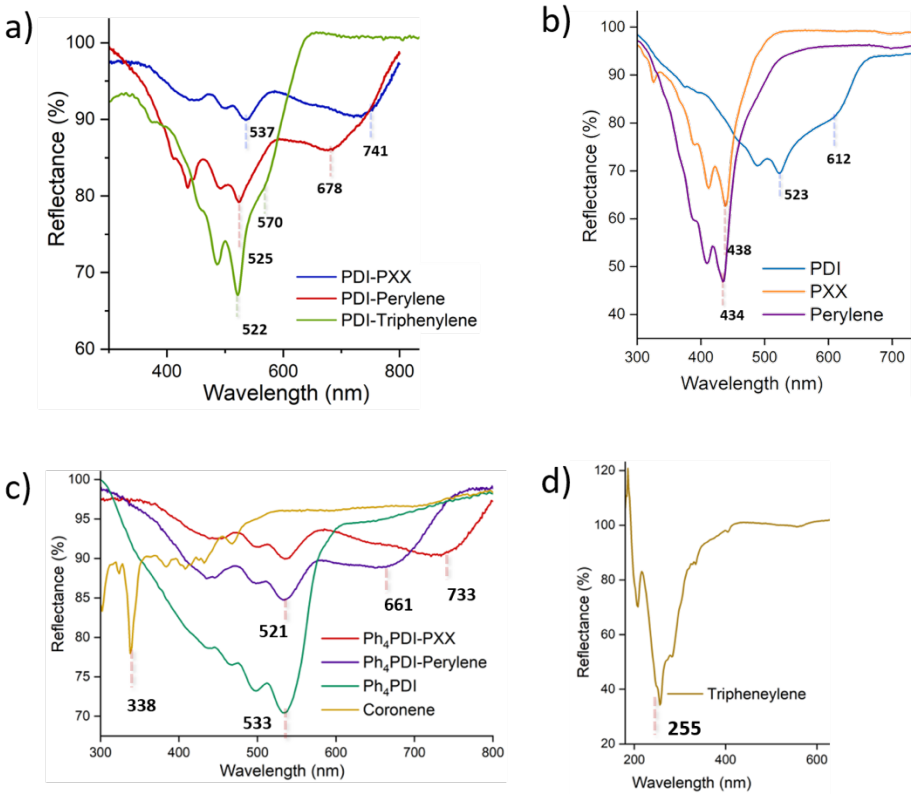

Figure 6: UV-Vis diffuse reflectance spectra for individual monomers and dimers of different PDI:donor and Ph_4PDI:donor co-crystals.

UV-Vis and near-IR spectra of Ph_4PDI, coronene, PDI, PXX, perylene, triphenylene, Ph_4PDI:PXX, Ph_4PDI:perylene, PDI-PXX, PDI:perylene, and PDI:triphenylene were acquired in diffuse reflectance mode. Samples were finely ground and mixed with MgO powder (~40 mm particle size) to make ~1 wt% mixtures. Sample mixtures were then pressed against a CaF_2 window mounted onto the side of a 100 mm integrating sphere. The measurements show that the PDI:PXX and PDI:perylene samples exhibit CT bands at 741 and 678 nm, differing from the pure monomers PDI,

PXX, and perylene (Figure 6a). PDI:triphenylene samples exhibit shorter wavelength CT features at 570 nm compared to PDI:PXX and PDI:perylene (Figure 6b, Figure 6d). A similar trend is observed in the case of Ph_4PDI:PXX and Ph_4PDI:perylene dimers. The CT band for Ph_4PDI:PXX is observed at a longer wavelength (733 nm) compared to Ph_4PDI:perylene (661 nm), as seen in Figure 6c. The diffuse reflectance spectra of the dimers are different from the spectra measured for individual monomers of PXX, perylene and Ph_4PDI. We also synthesized other D-A co-crystals, including PDI:coronene, PDI:pyrene and Ph_4PDI:pyrene, as depicted in Figure 7. To isolate single crystals, the acceptor (PDI, 0.01 mmol or Ph_4PDI, 0.01 mmol) and donor (pyrene or coronene, 0.01 mmol) molecules were mixed in a 1:1 ratio in a 4 ml glass vial and heated at 80 °C for 20 mins. For these three co-crystals, a toluene/methanol mixture was used as a solvent at a 3:1 ratio (2 ml). After the solution became clear, the vial was left at RT for slow evaporation. SCXRD was used to characterize the structures. PDI:coronene and PDI:pyrene crystallize in a P-1 space group, while PDI:pyrene crystallizes in $P2_12_12$ crystal system. These crystals form in a 1:1 ratio, with donor and acceptor packed one above the other through π-π stacking interactions with interatomic distances of 3.413, 3.536 and 3.496 Å for PDI:coronene, PDI:pyrene and Ph_4PDI:pyrene, respectively (Figure 7). The other characterization measurements such as PXRD, TGA, and UV-Vis are underway.

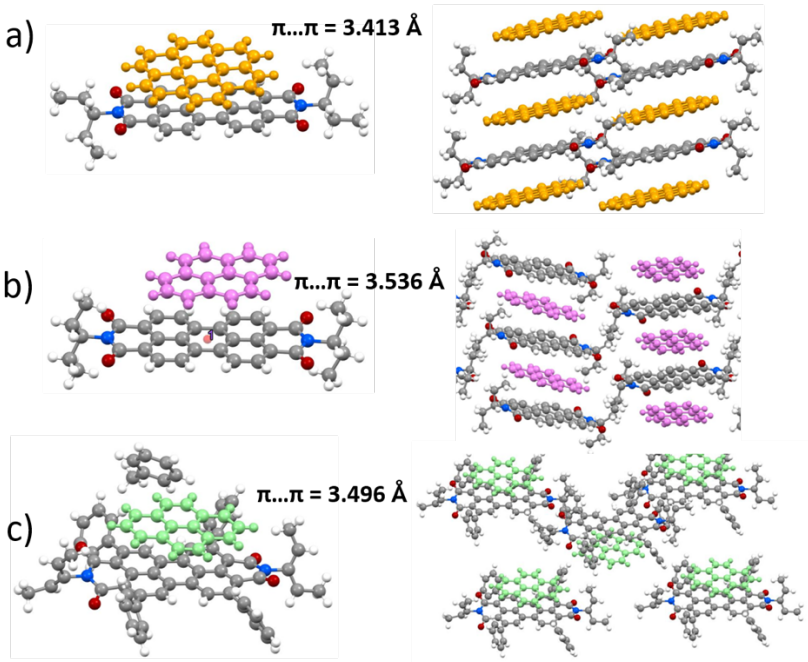

Figure 7: Structural representations of co-crystals a) PDI:coronene, b) PDI:pyrene and c) Ph_4PDI:pyrene.

2.1.2. Preparation of Npe:TCNB dimer solutions

To prepare solutions of the D-A dimers, 40 mmol solutions of Npe and TCNB in 1,4-dioxane were prepared separately. Equivalent volumes were mixed together to form Npe:TCNB dimers. The clear solutions turned yellow upon mixing, indicative of dimer formation.

2.1.3. Confining and characterizing D-A pairs in MOFs

The confinement of D-A pairs within crystalline porous materials such as metal-organic frameworks (MOFs) has rarely been explored but offers a route to precise studies of the role of D-A orientation

and environment on CT exciton dynamics for improved optoelectronic device design.[15] Confinement of D-A pairs in different MOFs may also enable tunability of band gaps through different orientations and interactions with the environment. To date, there are more than 80,000 MOF structures that have been reported in literature, allowing us to select several suitable candidates that will properly confine D-A pairs, which depends on the stability of the MOF, size and shape of the MOF pore, and ease of synthesis and D-A capture. Here we focused on confinement of TCNQ:napthalene and TCNQ:pyrene. MOF-177 was selected because it can be synthesized easily in a single crystal form and has pore sizes that can accommodate our chosen guest molecules. SCXRD and electron microscopy were used to verify the phase purity and the size, shape, and morphology of the MOF crystals. After synthesis of MOF-177, the original solvent was exchanged with DCM. Then, MOF single crystals were soaked in solutions of 0.04:0.04mmol TCNQ:napthalene (1:1) and 0.04:0.04mmol TCNQ:pyrene (1:1). After a couple of days, the crystals were filtered and washed with solvent to remove the surface adsorption of acceptor or donor molecules or solvent. To create reference samples, the same procedure was repeated to confine individual molecules (TCNQ, pyrene, and naphthalene) to obtain TCNQ@MOF, pyrene@MOF and napthalene@MOF composites. As shown in Figure 8, the color of the crystals changes after introduction of the D-A pairs, clearly indicating a difference between the confinement of individual monomers and the confinement of D-A dimers.

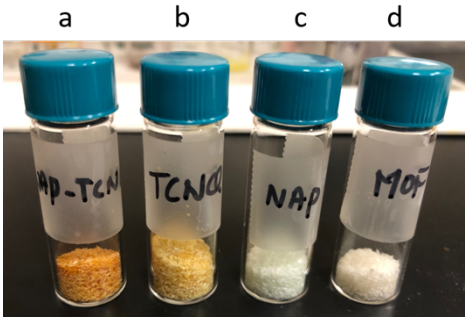

Figure 8: a) MOF-177+TCNQ:naphthalene, b) MOF-177+TCNQ, C) MOF-177+ naphthalene, and d) MOF-177.

To confirm the presence of guest molecules inside the host we measured the ^{1}H NMR spectra, as shown in Figure 9. In a typical experiment, filtered crystals were soaked in an NMR solvent for 1-2 hours. The supernatant solution was then measured with ^{1}H NMR to probe for leaching of the adsorbed molecules. These measurements indicate that both acceptor and donor (TCNQ:napthalene and TCNQ:pyrene) molecules were present in solution. The initial measurements indicate that the ratio of TCNQ:naphthalene is close to 3:1 (Figure 9a). In the case of TCNQ:pyrene the ratio was found to be 1:6.5 (Figure 9b). We also measured the reference samples (MOFs imbued with TCNQ, pyrene, or naphthalene), which revealed the presence of these molecules. We conducted SCXRD measurements to obtain the crystal structures of the D-A dimers embedded in the MOFs. While these studies are only preliminary, we see evidence of the presence of guest molecules in the MOF pores. One example of this is that in TCNQ:naphthalene in MOF-177, the naphthalene can be easily identified in the MOF pore from the difference in electron density maps; the remaining high electron density may correspond to TCNQ. Unfortunately, our repeated attempts to solve the

crystal structure have been unsuccessful so far and higher resolution measurements at synchrotron sources may be required.

Another technique employed to find evidence of D-A pairs in MOF pores is UV-Vis diffuse reflectance spectroscopy, as shown in Figure 10. These spectra show the absorption bands of individual monomer vs. D-A pairs embedded in the MOFs. When individual monomers are confined within MOF pores, a strong band is observed at 624 nm for pyrene@MOF and 446 nm for naphthalene@MOF. This indicates that at these wavelengths, there is a strong interaction between these individual molecules and MOF. In TCNQ@MOF, broad bands are observed at 755 and 600 nm. Interestingly, when D-A pairs present in the MOF, there are observable shifts compared to their constituent monomers, likely due to CT interactions. More studies are underway to characterize these features.

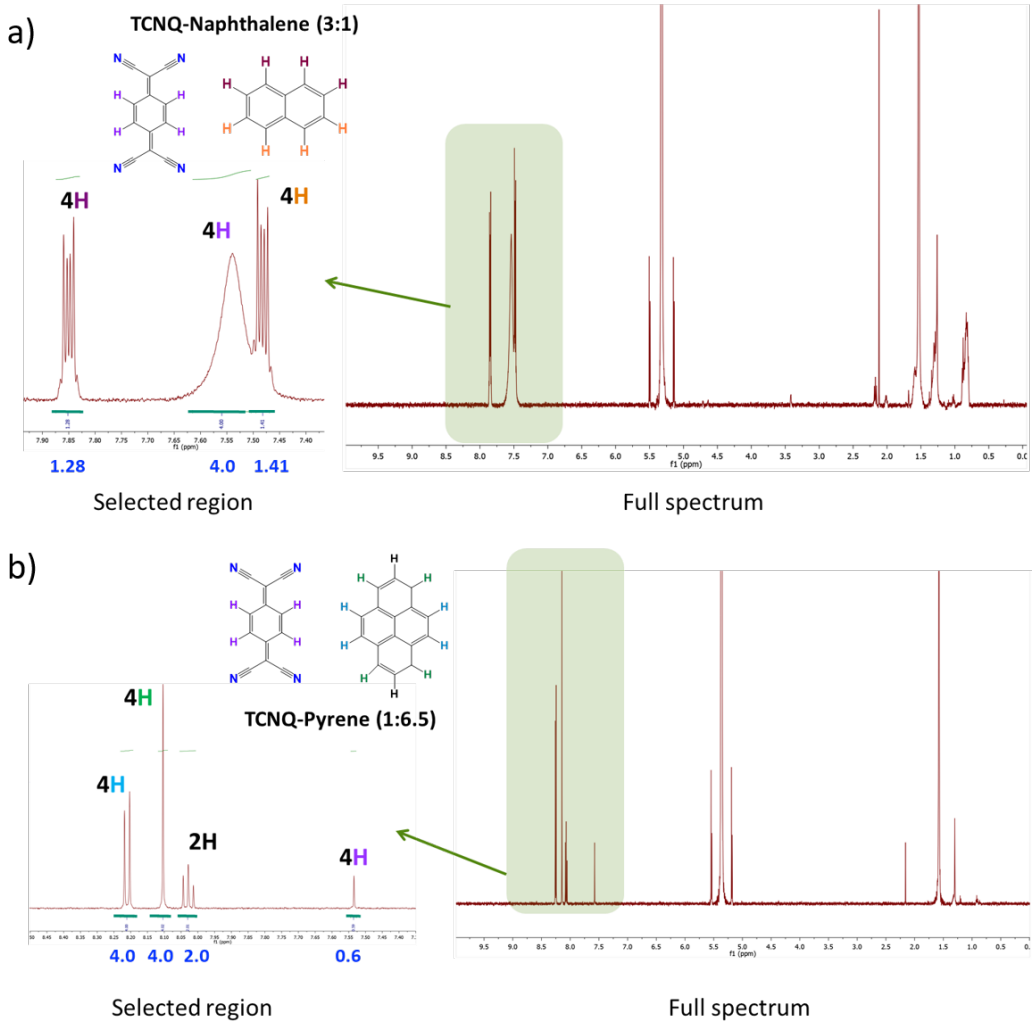

Figure 9: ^{1}H NMR measurements to confirm the presence of D-A pairs, a) TCNQ:napthalene and b) TCNQ:pyrene.

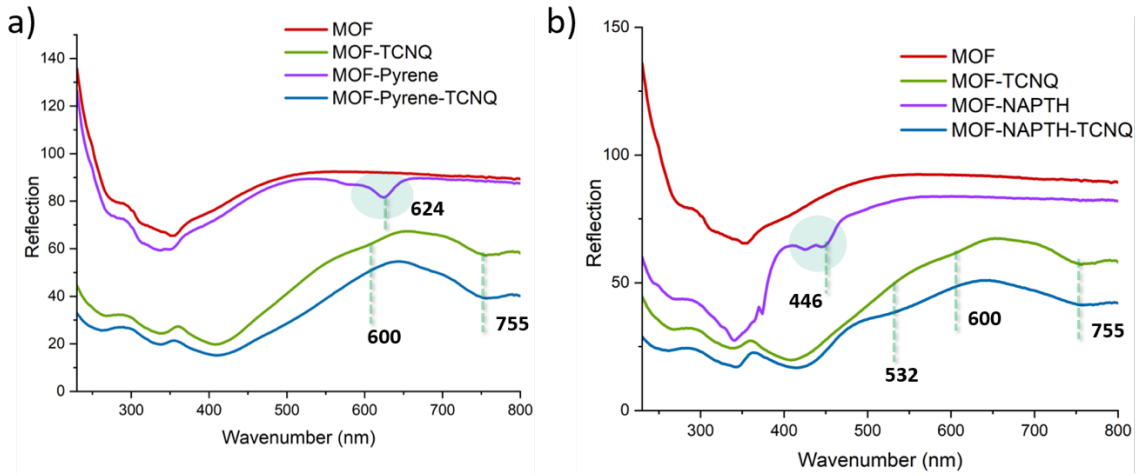

Figure 10: UV-Vis diffuse reflectance spectra measured for MOF, monomers@MOF, and D-A@MOF.

2.2. UV pump, UV-Vis probe TAS and characterization

2.2.1. TAS of Npe:TCNB co-crystals and dimers

The UV pump, UV-Vis probe TAS set-up that carried out transient measurements on co-crystals is described here. A 780 nm, 0.8mJ, 1 kHz, 55 fs output from a Ti:sapphire regenerative amplifier (Wyvern 1000, KM Labs) is chopped at 500 Hz and is then divided into two beams (95:5). The former is used to generate a 400 nm pump beam and the later to generate a broadband white light probe, spanning 350-800 nm. Approximately 0.04 mJ of the fundamental is focused on to a 1 mm thick CaF_2 window to generate a white light continuum which is then collimated by an aluminum parabolic mirror. Using an 8" aluminum parabolic mirror, the probe gets focused to a 60 µm ($1/e^2$) spot at the sample and reaches the sample at a 90-degree angle of incidence. The transmitted probe is collimated using an achromatic lens and sent to a spectrometer (OceanFX Spectrometer). The remaining 0.75 mJ arm is chopped at 250 Hz and sent through a half waveplate and linear polarizer combination, which provides control over pump energy, and then is optically delayed using a retroreflector mounted on a motorized stage. A BBO crystal (BBO-603H, Eksma Optics) generates the 400 nm pump beam via second harmonic generation. The pump is then focused to a 200 µm ($1/e^2$) spot, where both pump and probe beams are focused, and spatially overlapped on the sample. Both pump and probe beams intersect at their focal points, where the cocrystal sample resides on a manual stage which can be moved along three perpendicular axes. A pump fluence dependent study was carried out to identify the range of fluences in which the co-crystal absorption exhibits linear response. A pump fluence of 160 µJ cm^{-2} was used. In the TAS experiments, two different probe intensities are collected for each time delay: first, when both pump and probe are incident on the sample and second, the pump is blocked so that only the probe is incident on the sample. The difference between these two probe intensities provides the transient spectrum:

$$\Delta mOD = -\log\left(\frac{I_{pump.on}}{I_{pump,off}}\right) * 10^3 \quad (1)$$

where $I_{pump,on}$ and $I_{pump,off}$ are the flux of the probe transmitted through the sample, with and without exposure from the pump beam, respectively.

A different commercial laser set-up (Legend Elite, Coherent) was used to carryout UV pump, UV-Vis probe TAS experiments on the D-A dimer solutions. An 800 nm, 1.5 mJ, 1 kHz, 35 fs output of a regenerative amplifier is split into two beams; 80:20 to generate the pump and the probe respectively. The optical layout is like the layout described above except for following. The repetition rates of the pump and probe are 500 Hz and 1000 Hz, respectively. A 2 mm thick CaF_2 [001] single crystal is used for white light generation. Dimer solutions are placed in a 1 mm path length, 300 µL, quartz cuvette which is rastered continuously throughout the experiment. The pump fluence was set to 750 µJ cm^{-2}.

The inherent chirp observed in the TAS data was corrected by fitting the position of time-zero to a third order polynomial. The global fit analysis of the transient data was performed using KiMoPack[16] software package which numerically fits kinetic rate equations with the data. Singular value decomposition (SVD) was applied to identify the number of spectrally and temporally independent components. As shown in Figure 11, the data can be well-described by three main components. The first component dominates the overall signal while the remaining two components have much smaller contributions. A three-component model provides good agreement with our experimental data; we see negligible improvement with higher order fits. Hence, we only considered kinetic models with three or fewer components. Each kinetic model was convoluted with a Gaussian instrument response function (IRF) with full-width half maximum (FWHM) of 90.76 ± 18.04 fs to account for instrument resolution. To avoid fitting coherent artifacts that arise during pump-probe overlap, which are present past the IRF, only the transient data after 200 fs were fit to kinetic models.

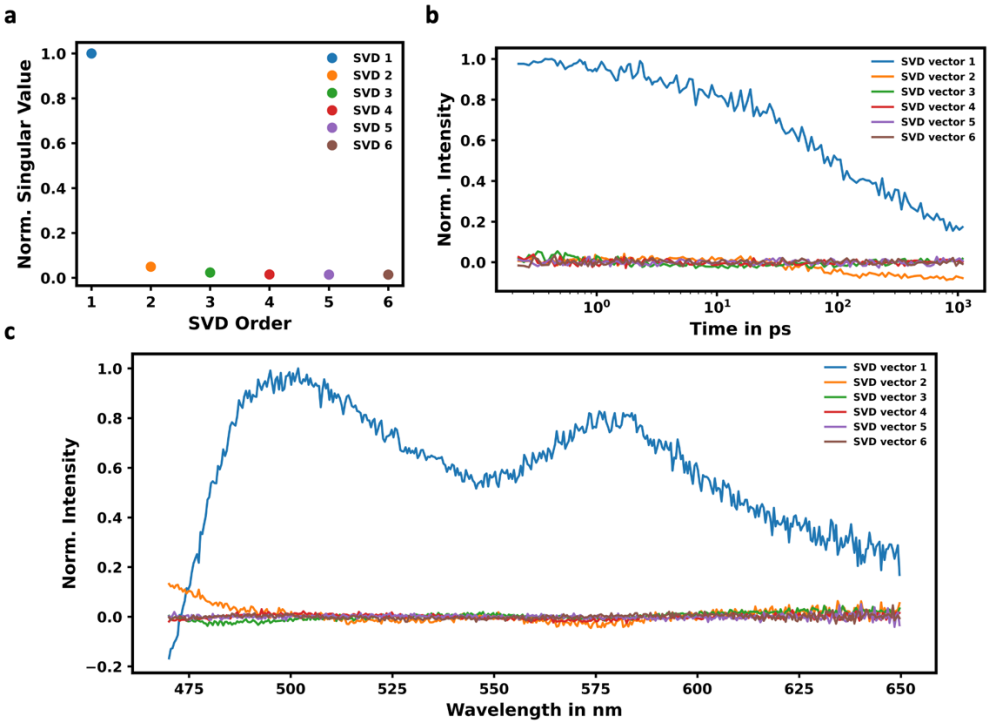

Figure 11: SVD analysis of Npe:TCNB TAS data. a) SVD Component strength, b) Temporal development of SVD, c) Spectral components from SVD analysis.

2.2.2. TAS of co-crystals with a PDI acceptor

A detailed description of the UV pump, UV-Vis probe TAS setup is provided elsewhere.[17] Briefly, the output of a LIBRA Ti:Sapphire regenerative amplifier (Coherent) with a ~800 nm center wavelength, 45 fs pulse duration and 1 kHz repetition rate is used as the fundamental beam. A large fraction of this is sent through an optical parametric amplifier (OPerA Solo, Coherent) to generate the tunable pump, which is then sent to a commercial transient absorption spectrometer (Helios, Ultrafast systems). The broadband probe beam (420-760 nm) is generated inside the transient absorption spectrometer by focusing a small fraction of the power of the fundamental beam into a sapphire window. The differential absorption signal induced by the pump excitation of the sample is calculated as shown above in Eqn. 1. Chirp correction for all data was performed using Surface Xplorer software (Ultrafast Systems) and kinetic analysis and data fitting were performed using the KiMoPack python package.[16] The kinetic fits were convoluted with a Gaussian IRF with FWHM of 600 fs. To avoid fitting coherent artifacts that arise during pump-probe temporal overlap, only the transient data after 1 ps time delay were fit using kinetic models.

2.3. Computational Methods

2.3.1. Npe:TCNB

The Npe:TCNB dimer was optimized using density functional theory (DFT) with the CAM-B3LYP functional,[18] 6-31G(d) basis set,[19, 20] and Grimme D3 dispersion correction[21] needed for the calculation of non-covalent interactions. Standard methods were used for optimizing the molecular geometries of the Npe:TCNB dimer conformers; frequency analysis was employed to ensure that geometries are minimum structures. Excited state calculations were carried out using the linear response time-dependent DFT (TDDFT) formalism.[22-24] These calculations were carried out using the Gaussian suite of electronic structure programs, G16.[25] In this section, non-adiabatic ab initio molecular dynamics (AIMD) calculations were conducted using the fewest-switches surface hopping approach[26] implemented in Newton-X CS software version 2.4 (build 06).[27] The initial conditions for dynamics were sampled from a harmonic oscillator Wigner distribution of the nuclei in the gas phase at 300 K.[28] 20 trajectories were propagated for 1000 femtoseconds (fs) with a 0.5 fs time step. The DFT and TDDFT calculations were performed on-the-fly at the CAM-B3LYP-D3/6-31G(d) level of theory, interfacing with Gaussian G16.

To compute the effects of vibrational broadening on the TAS spectra in the S_0, S_1, and T_1 states, we computed the oscillator strengths between the reference (S_0, S_1, and T_1) state and other electronic states in the energy range of the experiment at intervals of 25 fs. We assume that the vibrational broadening is well represented by the dynamics on the S_1 only and used only S_1 dynamics to broaden the spectra, even when computing the TAS oscillator strengths with S_0 and T_1 as reference states. For the S_1 reference state, these oscillator strengths were computed with the Initial Maximum Overlap Method (IMOM),[29, 30] as implemented in Q-Chem 5.4.[31] The IMOM technique is part of a broader category of Δ Self-Consistent Field (ΔSCF) methods, which adjust the orbital occupancies to mimic an excited state. Using the IMOM's solution for the reference first excited singlet state (S_1), we performed TDDFT calculations on top of this reference to determine vertical excitation energies and oscillator strengths for transitions from S_1 to higher excited states (S_n). Standard TDDFT methods were used to compute the TAS spectra for the ground singlet state (S_0) and the lowest-lying triplet state (T_1). We compare the TAS spectra in the gas phase and with the effects of 1,4-dioxane, employing the SMD universal solvation model[32] as implemented in QChem 5.4.[33]

2.3.2. PDI Acceptors

The electronic structure and dynamics of donor:PDI systems were computed in the same manner as the Npe:TCNB (Section 2.3.1). In some cases, different functionals were used, as marked throughout Section 4.

2.3.3. Assessing metrics for quantifying charge transfer

A variety of density functional/basis set combinations were used to quantify the degree of CT (DCT). All structures were optimized using CAM-B3LYP-D3/6-31+G(d,p).[18, 19, 21] Additional single-point calculations were carried out using the ωB97X-D,[34] APF-D,[35] PBE1PBE-D,[36, 37] and M062X[38] functionals. In all cases, the Grimme D3 dispersion correction was used except for M062X, which has a built-in dispersion correction.[39] All additional basis sets, 6-31G[40] and 6-311++G(3df,3pd),[41-43] were also employed alongside the ωB97X-D functional. All calculations were carried out using the Gaussian suite of electronic structure programs, G16.[25] Standard methods were used for optimizing the molecular geometries of the Npe:TCNB dimer conformers; frequency analysis was employed to ensure that geometries are minimum structures. Excited state calculations were carried out using the linear response time-dependent DFT (TDDFT) formalism.[22-24] Based on our previous recommendation,[44] the DCT is calculated using transition density matrix (TDM) analysis in Theodore.[45] The spatial overlap metric, Λ,[46] is calculated using the Multiwfn program.[47]

3. CT EXCITON DYNAMICS OF NPE:TCNB

3.1. UV pump, UV-Vis probe ultrafast TAS

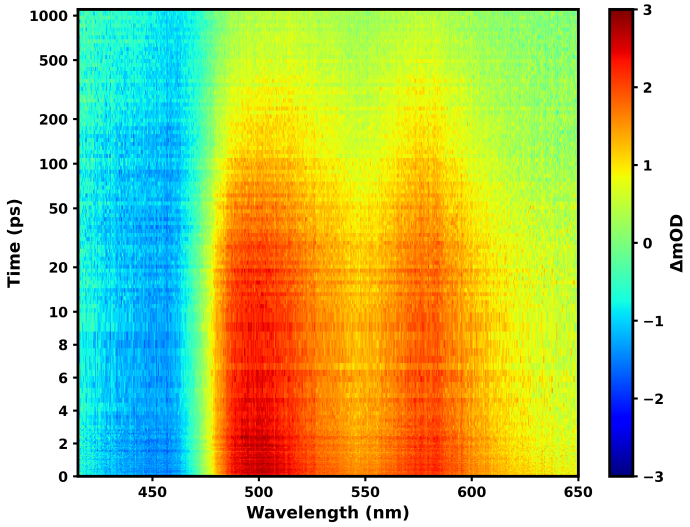

Figure 12: Ultrafast UV pump, UV-Vis probe TAS of the Npe:TCNB co-crystal. Differential absorption (ΔmOD) is shown as a function of wavelength and time in ps.

Our previous, published work on the Npe:TCNB cocrystal shows that the calculated S_1 state is centered at 430 nm and can be characterized as a CT HOMO → LUMO transition from Npe to TCNB. 33) In the experimentally obtained UV-Vis diffuse reflectance spectrum, this transition occurs at 450 nm. Due to constraints in our experimental setup, in the UV pump, UV-Vis probe TAS experiments, we use a slightly blue shifted 400 nm pump beam to excite this S_1 state. Due to the broadness of the S_1 feature, 400 nm can directly excite this CT S_1 state. After excitation to the S_1 state, time-resolved broadband UV-Vis probe pulses report on the correlations between the system's present electronic state and other electronic states within the energy range of the probe. Figure 12 shows the time-dependent spectral changes occurring in the Npe:TCNB co-crystal. Initially, a strong negative absorption appears around 450 nm, corresponding to the ground state bleach (GSB). This feature arises due to the depletion of the ground state population due to excitation from the 400 nm pump. The GSB feature is present for the entire time of the experiment, though a slow recovery is observed. The GSB feature at long timescales indicates the existence of a long-lived excited state. Two dominant positive features are centered near 500 nm and 580 nm, which we attributed to excited state absorption (ESA), likely from the S_1 state. Both bands persist over an extended timescale (> 50 ps), which is also an indication of long-lived excited states.

3.2. Kinetic fitting of TAS data

As commonly seen in D-A co-crystals, the excited electron and hole pairs generated upon photoexcitation are bound and give rise to a quasi-particle called an exciton.[48] Since we directly photoexcite a CT band, the initial state formed is a CT singlet exciton.[48] This CT exciton can change electronic character, relax radiatively or nonradiatively, combine with other excitons and undergo exciton-exciton annihilation (EEA), or move across the co-crystal. Due to the many possible exciton dynamics mechanisms, the assignment and fitting of a kinetic model is very challenging. We have performed SVD analysis (Figure 11) on the Npe:TCNB TAS data and concluded that a three component model best describes the dynamics. Based on this analysis, we have identified three candidates for kinetic models: a) First-order decay (Equations 2, 3), b) First- and second-order decay (Equations 4, 5), and c) A branched model (Equations 6, 7) that involves intersystem crossing (ISC).

$$[CT_{S1}] \xrightarrow{k1} [GS] \tag{2}$$

$$\frac{d[CT_{S1}]}{dt} = -k_1[CT_{S1}] \tag{3}$$

$$[CT_{S1}] \xrightarrow{k1+k2} [GS] \tag{4}$$

$$\frac{d[CT_{S1}]}{dt} = -k_1[CT_{S1}] - k_2[CT_{S1}]^2 \tag{5}$$

$$[CT_{S1}] \xrightarrow{k1} [GS] \tag{6}$$
$$[CT_{S1}] \xrightarrow{k2} [T_n] \xrightarrow{k3} [GS]$$

$$\frac{d[CT_{S1}]}{dt} = -k_1[CT_{S1}] - k_2[CT_{S1}] \tag{7}$$
$$\frac{d[CT_{T1}]}{dt} = k_2[CT_{S1}] - k_3[CT_{T1}]$$

3.2.1. First-order decay model

In the first-order decay model (Equations 2, 3), we considered only single-exciton decay pathways, where all underlying decay kinetics are wrapped into decay constant k_1. Performing a global fit of the experimental data (see Figure 13a), including GSB and both ESA features, we obtain a k_1 value of $3.52*10^{-2} \pm 1.35*10^{-4}$ ps^{-1}, corresponding to a t_1 value of 284.02 ± 0.00 ps. We find that a single exponential decay model is insufficient for globally fitting the data, as evidenced by significant deviations between the fit and experimental data for all three wavelengths reported, 450, 500, and 580 nm. Due to the poor fit of this data to a simple exponential decay, we turn to two more complex models that will enable incorporation of EEA processes and simultaneous parallel decay pathways.

3.2.2. First- and second-order decay model

When the organic D-A co-crystals are exposed to higher laser fluence, a larger density of excitons is generated, which increases the probability of two diffusing excitons coming into contact with each other. The interaction between two excitons can lead to EEA, resulting in recombination of at least one exciton to the ground electronic state. Due to the insufficient complexity of a first-order decay model in fitting the data, we include a second term in our kinetic model to describe EEA processes, as shown in Equations 4 and 5. We treat the EEA term, k_2, as being time independent, though others have treated this term as time-dependent.[11] When globally fitting the experimental data to this model (see Figure 13b), we obtain a k_1 rate coefficient of $3.76*10^{-6} \pm 1.30*10^{-10}$ ps^{-1} and a k_2 rate coefficient of $6.78*10^{-3} \pm 1.02*10^{-3}$ $(\Delta mOD*ps)^{-1}$. Because k_2 is a few orders of magnitude larger than k_1, we suggest that EEA is the dominant decay process at early times (< 50 ps), due to a higher exciton density, increasing the probability of diffused excitons interacting.[11] At later time delays, first order decay processes dominate as the exciton density lowers. This first- and second-order decay model offers a better fit compared to the simple first-order decay model, as evidenced

by a better fit of the ESA features (500 and 580 nm) in Figure 13b. However, this model still struggles to sufficiently capture the GSB feature (450 nm). We thus turn to a final branched, parallel-decay model to fit the data.

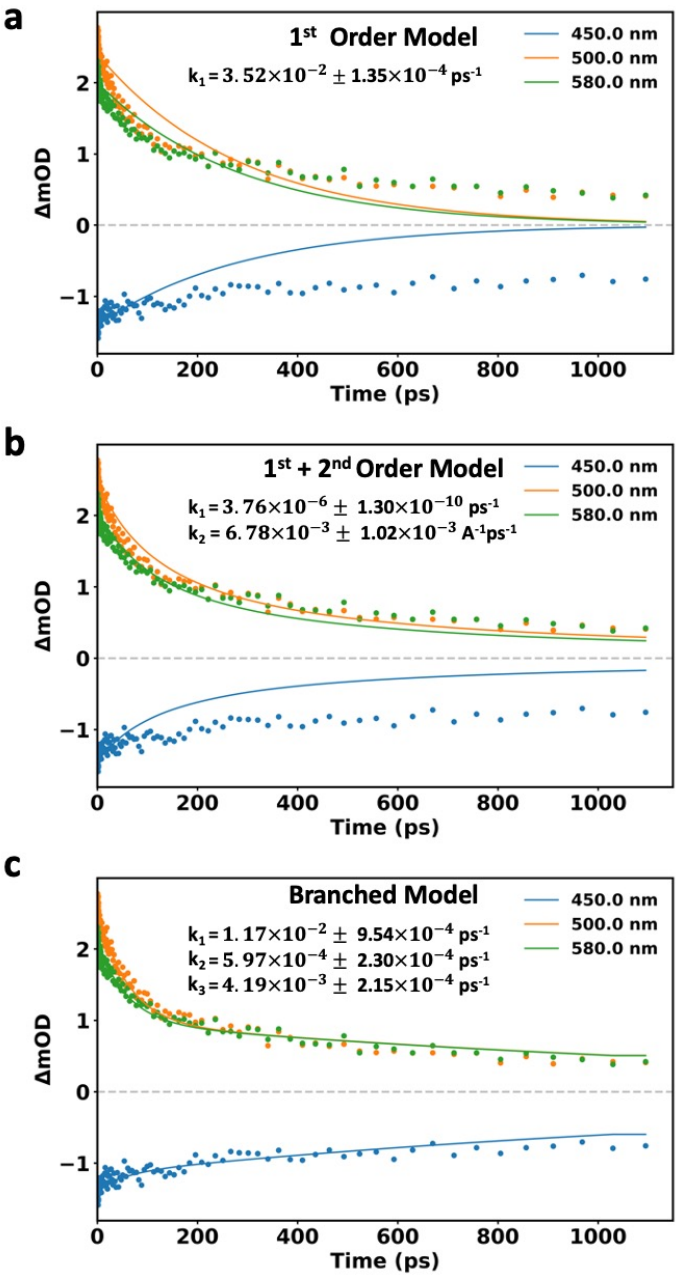

Figure 13: Plots of the fitted (solid) and experimental (dots) data at 450, 500, and 580 nm with fits given by (a) the first-order decay model, (b) the first- + second-order order decay model, and (c) the branched model.

3.2.3. Branched model

In TAS experiments of D-A co-crystals, ISC is often identified by shifts and changes to the time-resolved spectra.[49] This is because, in general, there are different electronic oscillator strengths and energy differences between the singlet states vs. the triplet states, resulting in distinct spectral features arising upon ISC. In our TAS data, we do not see any obvious shifts in the ESA features that enable clear assignment of ISC. However, this does not mean that ISC is not occurring. Due to the broad, overlapping ESA features, it is challenging to assign each feature as arising from one exciton relaxation process alone. Furthermore, the singlet and triplet features may look very similar. Based on the insufficiency of the previous two models, we consider a third, branched model that describes parallel singlet relaxation and ISC relaxation processes, given in Equations 6 and 7. Figure 13c shows the global fit of the data with this model, indicating values of $1.17*10^{-2} \pm 9.54*10^{-4}$ ps^{-1} for k_1, $5.97*10^{-4} \pm 2.30*10^{-3}$ ps^{-1} for k_2, and $4.19*10^{-3} \pm 2.15*10^{-4}$ ps^{-1} for k_3. The lifetime of the singlet CT exciton is given by $1/(k_1+k_3)$ and has a value of 324.17 ± 19.27 ps. The lifetime of the triplet exciton is given by $1/k_2$ and has a value of 1.68 ± 0.50 ns. Of the three models, this branched model captures the long-time behavior best. Due to the lack of spectral shifts that we can attribute to ISC, we turn to theoretical predictions of the TAS signatures arising from the S_1 and T_1 states of the D-A dimer system. We note that time-resolved electron paramagnetic resonance (TREPR) spectroscopy could be used in future studies to strengthen our assignment of ISC, as performed in other studies of the exciton dynamics of co-crystals.[49] We also note that in reality, many competing single- and multi-exciton processes are at play in the exciton relaxation dynamics of D-A co-crystals. However, for these TAS experiments we must use simple kinetic models to avoid overfitting the data.

3.3. Predicting TAS signatures using AIMD and electronic structure calculations

To gain further insights into the excited state dynamics of the Npe:TCNB dimers, we performed non-adiabatic AIMD simulations on the S_1 and S_0 surfaces. We used these dynamics calculations to compute the effects of vibrational broadening on the TAS spectra originating from the S_0, S_1, and T_1 states. The results of these simulations are illustrated in the heat maps in Figure 14, which depict the computed TAS arising from S_0, S_1, and T_1 reference states in vacuum and a 1,4-dioxane environment.

The non-adiabatic AIMD simulations are performed over a 1 ps timescale and find that the average time spent on the S_1 surface is 778 fs. Of the total 20 trajectories, 55% remained on the S_1 surface throughout the simulation. For TAS arising from the S_1 state (see Figure 14), a broad feature centered at ~500 nm is prominent, likely corresponding to the two bands observed experimentally in Figure 12. These peaks are predominantly arising from $S_1 \rightarrow S_7$-S_{10} and $S_1 \rightarrow S_{11}$-S_{17} transitions. A weak feature around 700 nm arises from $S_1 \rightarrow S_2$-S_5 transitions, which we do not observe in the experimental TAS of the co-crystal. This may be due to scattering effects and lower white light intensity at this wavelength. The TAS arising from the T_1 reference state exhibits a spectrum very similar to the S_1 reference. In this case, the 500 nm region is made up of signals from $T_1 \rightarrow T_8$-T_{11} and $T_1 \rightarrow T_{12}$-T_{17} transitions. The feature at 700 nm originates from $T_1 \rightarrow T_2$-T_6 and is significantly weaker than the 500 nm region. For the TAS arising from the S_0 reference, a blue shift from ~500 to ~400 nm is observed. However, we do not observe this experimentally. Comparing the spectra in vacuum and 1,4-dioxane, we find that the solvent increases the intensity of the 700 nm features in the S_1- and

T_1-originating spectra and narrows the ~450 nm band in the S_0-originating spectrum.

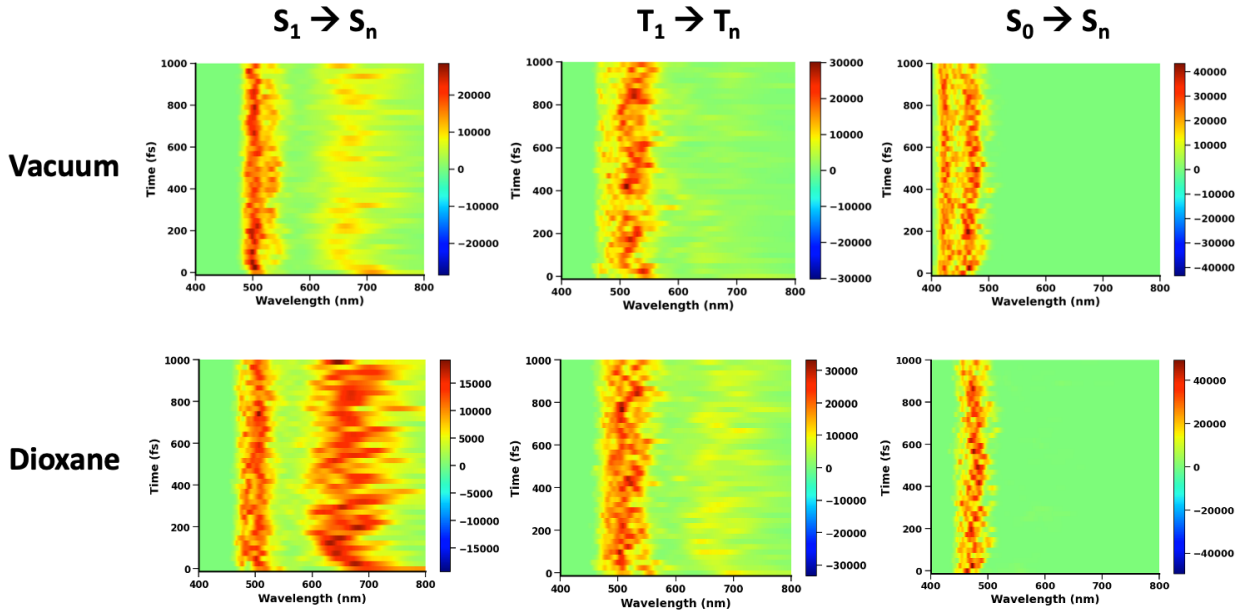

Figure 14: Simulated TAS of Npe:TCNB dimers in vacuum (top row) and 1,4-dioxane (bottom row) originating from the S_1, T_1, and S_0 states.

As explained above, determining exciton dynamics decay pathways is challenging in co-crystals, as multi-exciton pathways may contribute to the kinetics, which can be time-dependent.[11] Furthermore, the electronic structure of co-crystals becomes more complex in a drop cast samples with the emergence of multiple phases, grain boundary defects, or even intrinsic trapped states. We therefore compare the photoexcitation dynamics of the co-crystal with Npe:TCNB dimers in solution. The dimers were prepared in 1,4-dixoane, a solvent with relatively low polarity, to minimize the structural reorganization and CT between the photoexcited dimer and the solvent. Ultrafast TAS experiments were performed on Npe:TCNB dimers excited with a 400 nm pump and probed with broadband UV-Vis light. The TAS collected from these dimer solutions is presented in Figure 15a. A GSB feature appears near 400 nm and three broad ESA features emerge, centered around 465, 570 and 700 nm. It is important to note that the energies of GSB and ESA features are different between the dimer and co-crystal. A possible reason for this is differences in the electronic structure and electronic energy levels of the dimers vs. co-crystals. The dynamics of the two systems may differ because dimer and unbound monomers can interact with solvent molecules, creating more energy conversion pathways upon photoexcitation.

When the dimers are formed, they are in equilibrium with Npe and TCNB monomers. The static UV-Vis spectrum of Npe shows that both Npe and Npe:TCNB have S_1 states at similar energies, while the absorption of TCNB is more blue shifted. This implies that we are exciting both the dimer and Npe during TAS experiments. To evaluate the contribution from Npe, carried out a control TAS experiment with 40 mM Npe in 1,4-dioxane. Like the dimer, Npe has a GSB and three ESA features. We have compared spectral profiles of the dimer and Npe at different time delays in Figure 15b. On top of the broad absorption profile of Npe, the dimer has relatively narrow ESA features centered around 465 and 570 nm, with ESA lifetimes that are significantly prolonged compared to Npe.

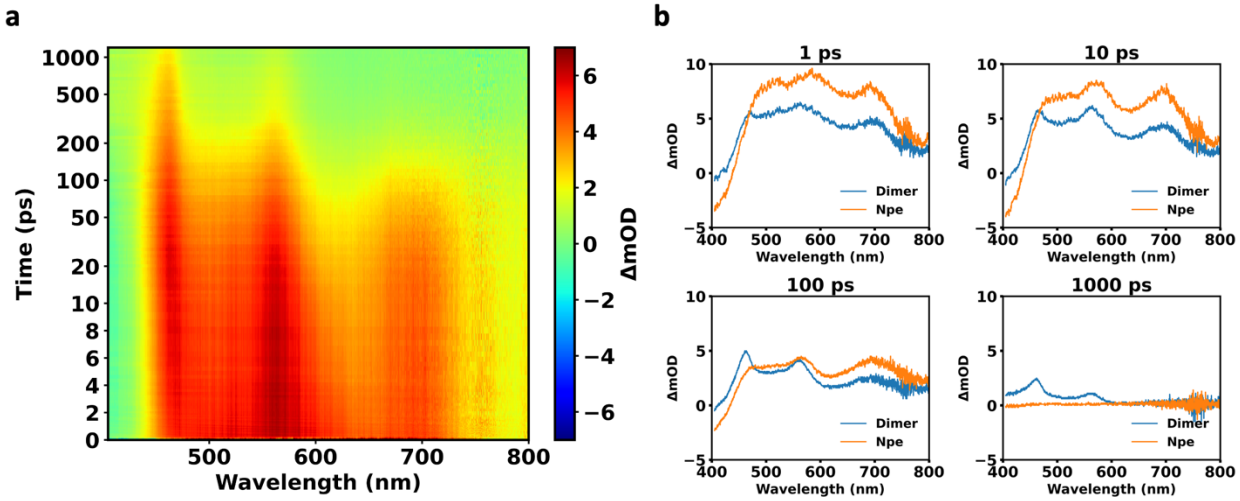

Figure 15: a) TAS of Npe:TCNB dimers in 1,4-dioxane, b) TAS lineouts of Npe monomer (orange) and Npe:TCNB dimer (blue) in 1,4-dioxane solvent at 1, 10, 100, and 1000 ps time delays.

4. CT EXCITON DYNAMICS OF CO-CRYSTALS WITH A PDI ACCEPTOR

4.1. Static UV-Vis Absorption Spectra

The static UV-Vis absorption spectra of PDI co-crystals are shown in Figure 16; the colored lines show pump spectra centered at 620, 650, and 570 nm, for PDI:PXX, PDI:perylene, and PDI:triphenylene co-crystals, respectively. The appearance of multiple absorption features in the ground state spectra for all three systems indicates that a manifold of valence band excitations is accessible in the UV-Vis region. However, it is important to note that drop cast co-crystals, such as those studied here, are inhomogeneous thin films that can scatter light, and a nonzero signal in the static absorption spectra does not necessarily correspond to the presence of a resonant absorption feature. The simulated ground state absorption spectrum of PDI:PXX given in Figure 19 suggest that the employed pump wavelength of 620 nm for this system excites the lowest singlet electronic excited state, S_1, assigned as a CT state due to the large degree of CT (see Figure 19). It is unclear from the theoretical absorption spectra (see Figure 20, Figure 25, and Figure 31) as to which states are being excited at the indicated pump wavelengths for PDI:perylene and PDI:triphenylene.

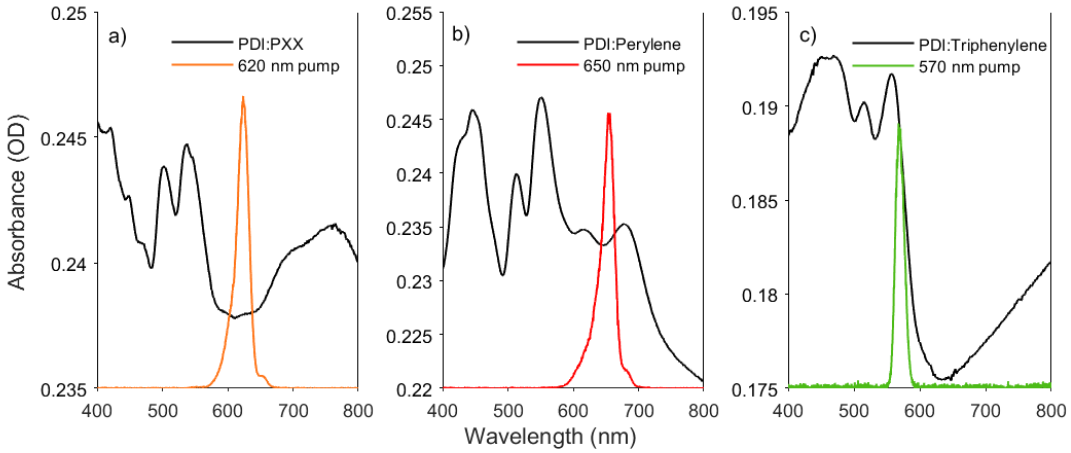

Figure 16: Static UV-Vis absorption spectra of a) PDI:PXX b) PDI:perylene and c) PDI:triphenylene co-crystals (black lines) and the respective pump excitation wavelengths (colored lines).

4.2. PDI:PXX

The PDI:PXX co-crystal was excited with a 620 nm pump, and Figure 17 shows the TAS following this excitation. A clear excited state absorption (ESA) feature centered around 740 nm is observed, which decays during the time span of the experiment (<8 ns). As the 740 nm ESA feature decays, two new ESA features near 700 and 750 nm emerge at longer time delays (> 1 ns), which do not decay within the experiment temporal window. We cannot extract any signal between 550-700 nm due to interference from pump scatter and there are no transient spectral features at wavelengths shorter than 550 nm.

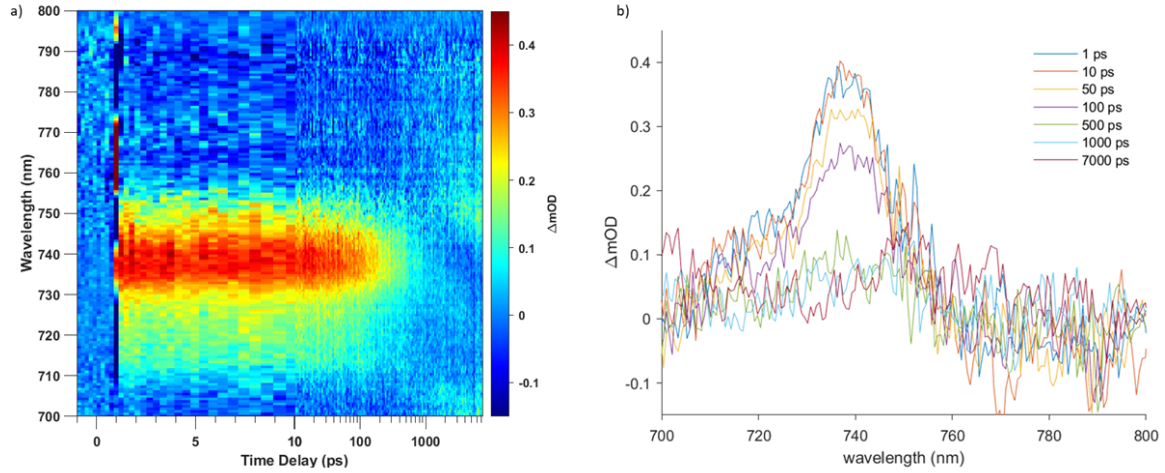

Figure 17: False color map of the TAS of PDI:PXX co-crystals, showing the differential absorption as a function of time delay and wavelength. b) TAS lineouts at select time delays.

To quantify the evolution of photoexcited states of PDI:PXX co-crystals, a global fitting analysis was performed for time delays from 1 to 7500 ps. The model that best describes the data is a two-step sequential kinetic model with a non-decaying component, given by

$$[A] \xrightarrow{k_1} [B] \xrightarrow{k_2} [C] \xrightarrow{1/\infty} \quad (8)$$

where A and B are the initial excited state species and an intermediate species, respectively, and k_1 and k_2 are decay rate constants of the A and B species. C is a long-lived species that does not decay within the experimental time window. Evolution associated difference spectra (EADS) predicted by the sequential model are given in Figure 18a. The spectral shapes of the EADS suggests that the initially excited species (A) almost fully decays to B, and only then is the red shifted non-decaying species C formed. The goodness of the fit to Equation (8) is shown in the form of kinetic traces of the ESA features centered at 740 and 752 nm in Figure 18b. The lifetime ($1/k_1$) associated with the initially excited species (A) is 279.86 ps, while the lifetime ($1/k_2$) of species B is 1396.66 ps.

A systematic exploration of the potential energy surface (PES) of the PDI:PXX dimer was conducted to identify the low-lying conformers, as shown in Figure 19. The structures of these conformers were compared with the experimental crystal structure (Figure 2); the relative energies of the different conformers were found to be very close. All conformers show a large DCT in the S_1 excited state S_1, while the S_0 ground state exhibits only a small DCT.

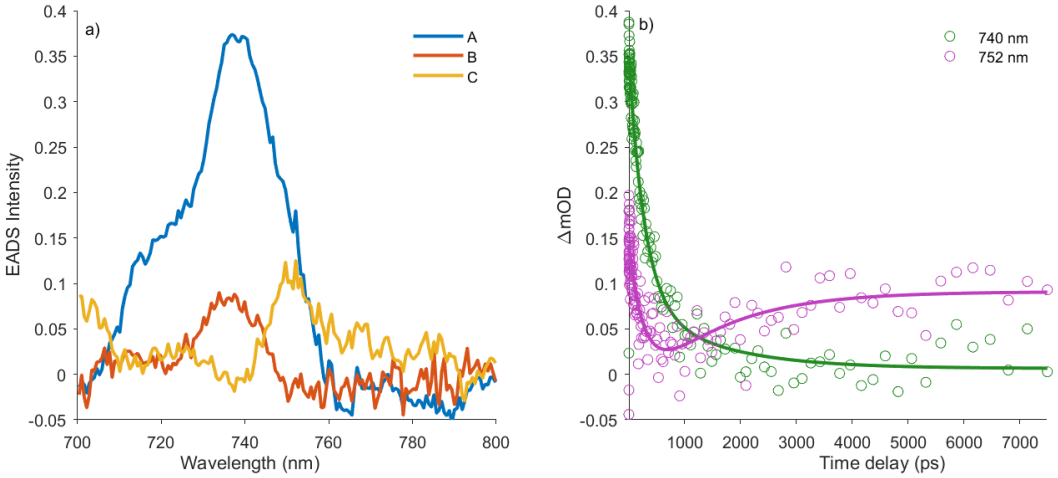

Figure 18: a) EADS corresponding to species A (blue), B (orange) and C (yellow). b) Kinetic traces at ~740 and ~752 nm from 1 to 7500 ps post-excitation. Circles represent experimental data, and solid lines represent fits obtained from global fitting.

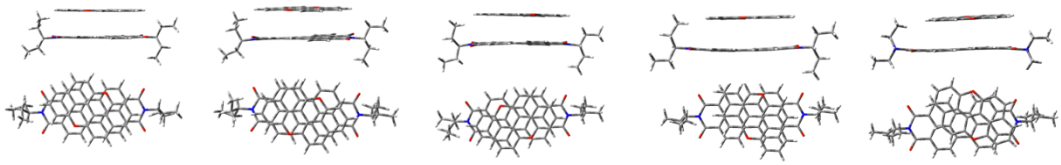

	1a	1b	1c	1d	CIF
$Energy_{rel}$ (eV)	**0.00**	**0.01**	**0.04**	**0.04**	
DCT in S_1 (e)	**0.95**	**0.95**	**0.98**	**0.98**	
DCT in S_0 (e)	**0.05**	**0.04**	**0.05**	**0.04**	
Osc. St. (au)	**0.05**	**0.05**	**0.05**	**0.004**	

Figure 19: Optimized geometries (1a–d) of PDI:PXX found with CAM-B3LYP-D3/6-31+G(d,p) and the experimental CIF structure. Energies (eV) are reported relative to the lowest-energy structure (1a) and include zero-point energy corrections. The calculated degree of CT is reported for S_0 and S_1, as well as the associated S_0–S_1 oscillator strengths.

The UV-Vis absorption spectra for the conformers were calculated and compared against experimental reflectance spectra, as shown in Figure 20. Overall, the theoretical spectra of all four conformers show reasonable agreement with experiment, although Conformer 1d does not exhibit the ~600 nm feature observed in the experimental data and other conformers' predicted spectra. Conformer 1a was chosen as the best model dimer structure, as it most closely resembles the experimental crystal structure. Overlaying its calculated UV-Vis spectrum with the experimental diffuse reflectance spectrum reveals good agreement.

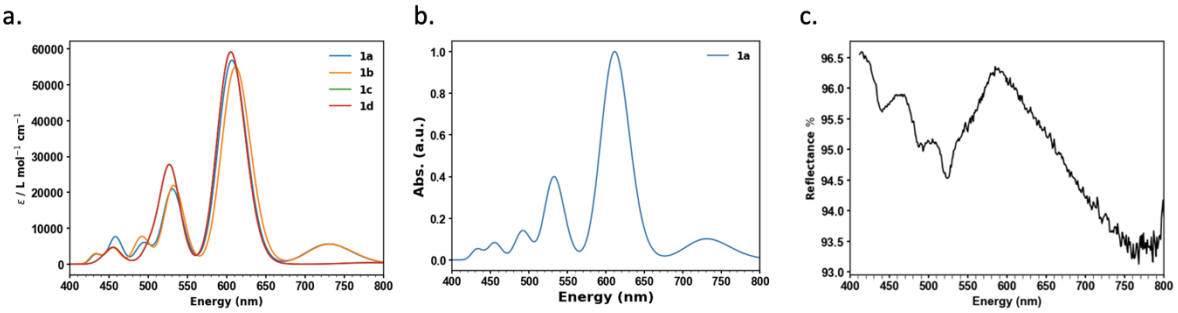

Figure 20: a) The simulated absorption spectra of PDI:PXX conformers a-d. b) The simulated absorption spectra of the best candidate for PDI:PXX conformer. c) Diffuse reflectance spectra of PDI:PXX.

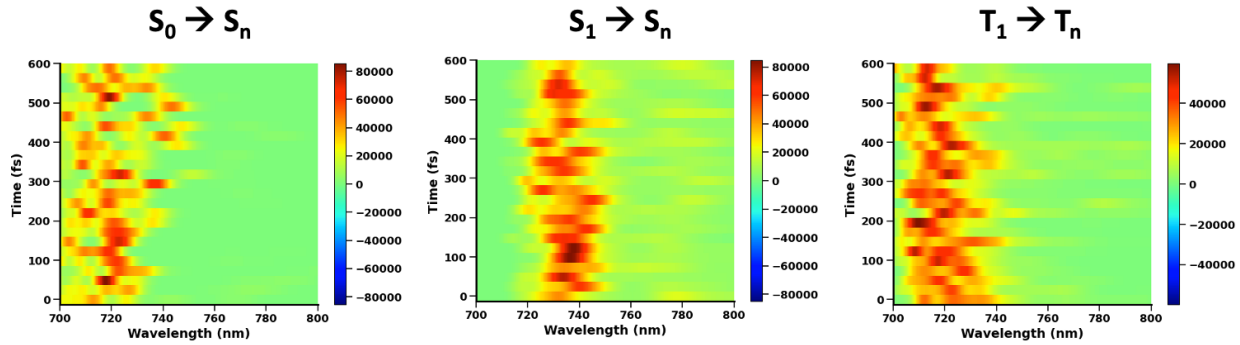

Figure 21: Simulated TAS of PDI:PXX dimers in vacuum originating from the S_0, S_1, and T_1 states.

We computed the TAS of PDI:PXX from non-adiabatic AIMD calculations arising from the S_0, S_1, and T_1 surfaces (Figure 21), as we did with Npe:TCNB. The experimental TAS (Figure 17) reveal a distinct feature around 740 nm, which decays rapidly within the first few hundred ps. In comparing the experimental and theoretical (S_1-originating) TAS, we observe that the 740 nm feature arises from S_1 to $S_{9\text{-}13}$ transitions. Although the timescale for the simulation is very short (1 ps) compared to the experiment, these dynamics act as a basis set, helping us to assign the spectra and choose kinetic models. The computational S_0- and T_1-originating TAS spectra show a dominant feature that is significantly broadened and blue shifted compared to what we observe in the S_1-originating TAS spectrum.

4.3. PDI:perylene

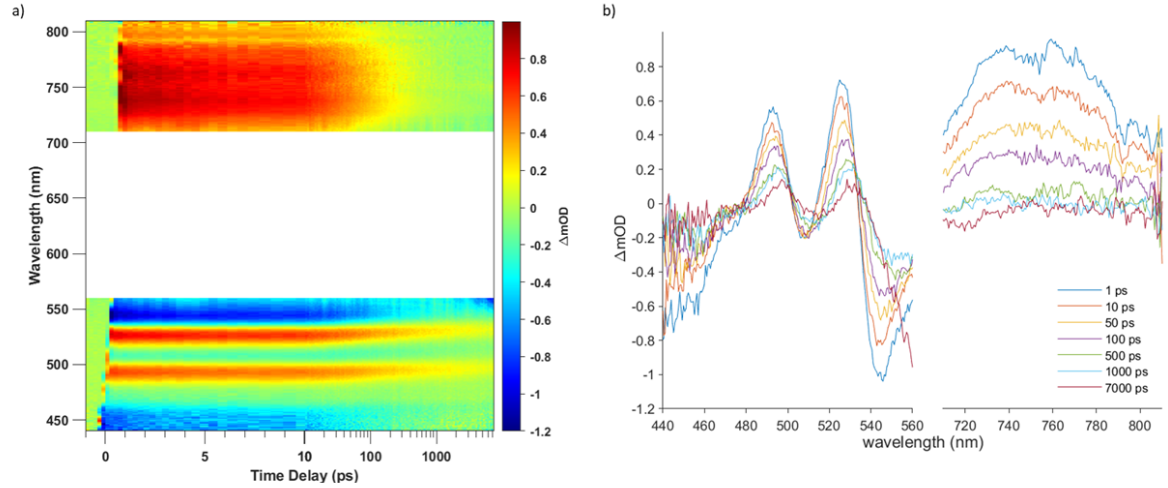

Figure 22: a) False color map of the TAS of PDI:perylene co-crystals, showing the differential absorption as a function of wavelength and time. The white area depicts the region of the spectrum that contains scatter from the pump pulse and hence cannot be interpreted. b) TAS lineouts at select time delays.

Figure 22 shows the TAS of PDI:perylene co-crystals upon 650 nm excitation; we have omitted the spectral range from 560-710 nm due to interference from pump scatter. We observe multiple ESA features: a broad positive feature spanning over 100 nm and centered around 750 nm, which decays within the experimental time window, and two more ESA features centered at 494 and 527 nm, which do not fully decay within 7.5 ns. The broad ESA feature centered at 750 nm decays faster than the sharp ESA features at shorter wavelengths; the latter two features begin to red shift at longer time delays (>100 ps). We observe three negative features in Figure 22 near 450, 510 and 542 nm. Their energies coincide with static absorption peaks shown in Figure 16, which suggests that these features are ground state bleach (GSB) features due to depletion of ground electronic state population after excitation. These GSB features decay on the same time scale as the short wavelength ESA features.

The kinetic model that best describes the data is given by Equation 8. Figure 23a displays the EADS of the three excited state species described by the model. Conversion from species A to B has a lifetime ($1/k_1$) of 31.84 ps and is represented by intensity decay in all ESA and GSB features. Species B has a lifetime of ($1/k_2$) of 411.45 ps and is converted to species C. The evolution of B to C is accompanied by a clear red shift in the short wavelength ESA features near 494 and 527 nm. Figure 23b shows the kinetic traces along several wavelengths as well as the fits obtained from the kinetic model, which faithfully represent the experimental data.

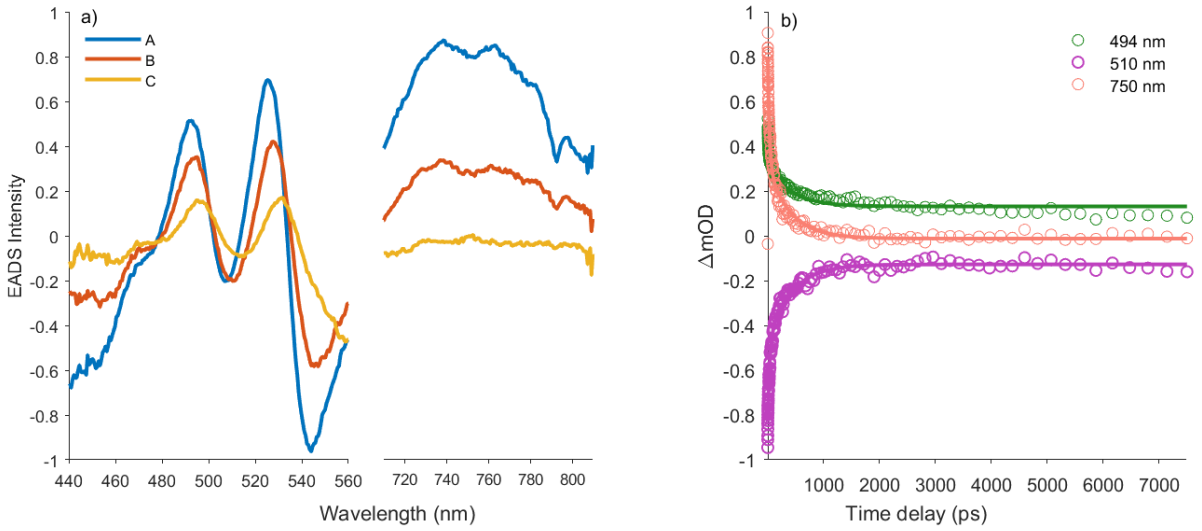

Figure 23: a) Evolution associated difference spectra corresponding to species A (blue), B (orange) and C (yellow). b) Kinetic traces at ~494 (green), ~510 (purple) and ~750 (pink) nm from 1 to 7500 ps post-excitation. Circles represent experimental data and solid lines represent fits obtained from global fitting.

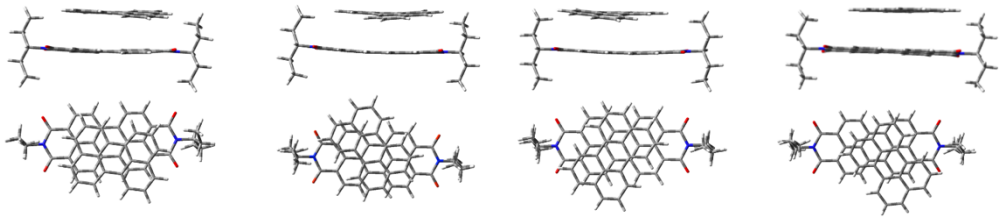

	2a	2b	2c	CIF
$Energy_{rel}$ (eV)	0.00	0.0007	0.0023	
DCT in S_1 (e)	0.94	0.98	0.98	
DCT in S_0 (e)	0.01	0.051	0.00	
Osc. St. (au)	0.031	0.006	0.008	

Figure 24: Optimized geometries (2a–c) of PDI:perylene computed with CAM-B3LYP-D3/6-31+G(d,p) compared to the experimental crystal structure. Energies (eV) are reported relative to the lowest-energy structure (2a) and include zero-point energy corrections. The calculated DCT is reported for S_0 and S_1, as well as the associated S_0–S_1 oscillator strengths.

The PDI:perylene dimer PES was explored and we identified three different low-lying conformers that we compare to the experimental crystal structure, as shown in Figure 24. The relative energies of these conformers were very close, indicating that rotation of the perylene yields conformers with very similar energies. When analyzing the DCT, we find that the S_1 DCT is greater than 0.94e for all conformers, which is almost complete electron transfer in the first excited electronic state. In contrast, the DCT in S_0 remained near zero for all conformers.

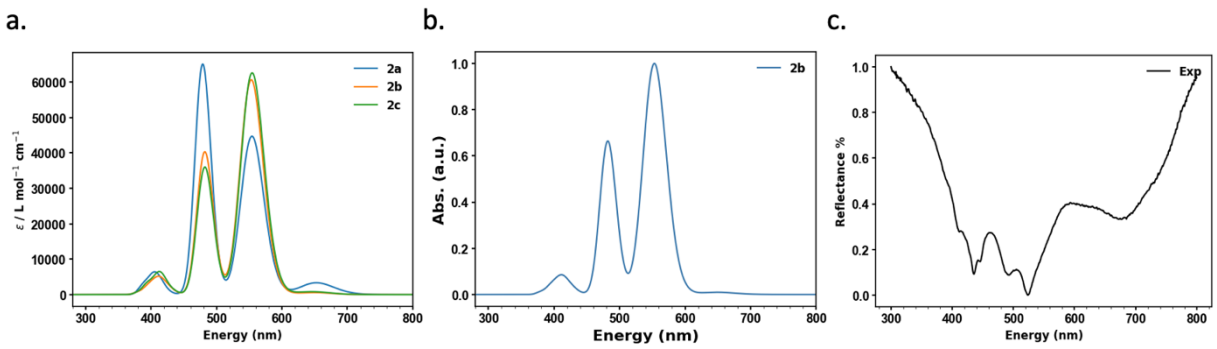

Figure 25: a) The simulated absorption spectra of PDI:perylene conformers, b) The simulated absorption spectra of the best candidate for PDI:perylene conformer, c) Diffuse reflectance spectra of PDI:perylene.

The calculated UV-Vis spectra for the PDI:perylene conformers were compared to experimental results, showing good agreement, Figure 25. All conformers exhibit a well-defined peak around 530 nm in the theoretical spectra, in agreement with the experimental feature at ~530 nm. The CT peak at ~650 nm has small oscillator strength in the theoretical dimer calculations in agreement with experiment. Conformer 2b is closest in resemblance to the experimental crystal structure, though there is a slight rotation difference between the two and is the chosen conformer for AIMD studies.

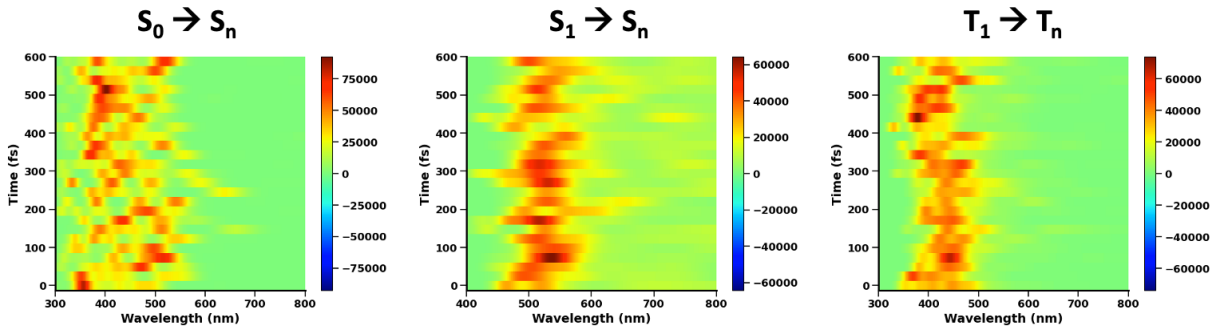

Figure 26: Simulated TAS of PDI:PXX dimers in vacuum originating from the S_0, S_1, and T_1 states.

To investigate the excited state dynamics of the PDI:perylene dimer, ultrafast TAS experiments were performed, as shown in Figure 22. Initially, a strong negative absorption appears around 420 nm, corresponding to the GSB. This feature arises due to the depletion of the ground state population due to the pump excitation and remains visible throughout the experimental timescale. Three dominant positive features emerge in the TAS bands centered near 480 nm and 530 nm, as well as a broad peak around 730-800 nm that we attribute to ESA from the singlet S_1 state. The first two bands persist over an extended timescale, indicating that they are integral to the relaxation dynamics of the system, while the broad peak has a weaker intensity and dies off on a faster timescale. We compute the TAS arising from the S_0, S_1, and T_1 states of the PDI:perylene dimer with AIMD, see Figure 26. The calculations arising from the S_1 state show a broad feature between ~450 and 550 nm in the range of the two experimental features at 480 and 530 nm. These peaks correspond to various transitions between S_1 and $S_{10\text{-}16}$ states. The computed T_1-originating TAS spectrum

resembles the S_1-originating spectrum with a slightly narrowed main feature. The computed S_0-originating TAS spectrum exhibits a very broad and low intensity feature between 300 and 550 nm.

4.4. PDI:triphenylene

The ultrafast TAS data of the PDI:triphenylene co-crystal upon 570 nm excitation is given in Figure 27. We observe a broad ESA feature that does not fully decay within the time range of the experiment. The ESA feature has some structure, consisting of multiple peaks on top of a broad positive feature. This could suggest that the probe interaction excites the initially pumped state to distinct manifolds of higher energy states that are close in energy. As we approach longer time delays, the sharper structures give way to three broad features. The spectral lineout at 7000 ps in Figure 27b shows that there is a slight red shift compared to early time delay spectra. Like the data shown in previous sections, transient signals for wavelengths shorter than 620 nm are obfuscated by the presence of pump scatter.

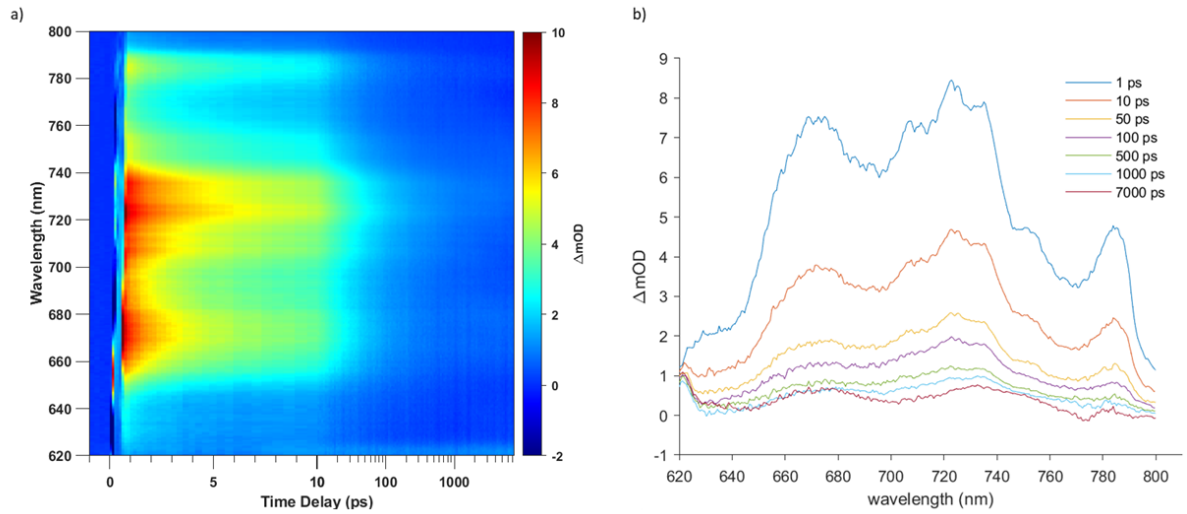

Figure 27: a) False color map of the TAS of the PDI:triphenylene co-crystal system, showing the differential absorption as a function of wavelength and time delay. b) Transient spectra at select time delays.

To quantify the time evolution of the ESA, we performed a global analysis on the TAS data. We first considered a two-step sequential model represented by Equation 8. The EADS in Figure 28a shows that the relative intensities between peaks around 660, 730 and 790 nm change when going from species A to B. The non-decaying species C does not show the sharp spectral features that are seen in the spectra of species A and B. The extracted lifetimes of species A and B are 5.55 ps and 97.74 ps, respectively.

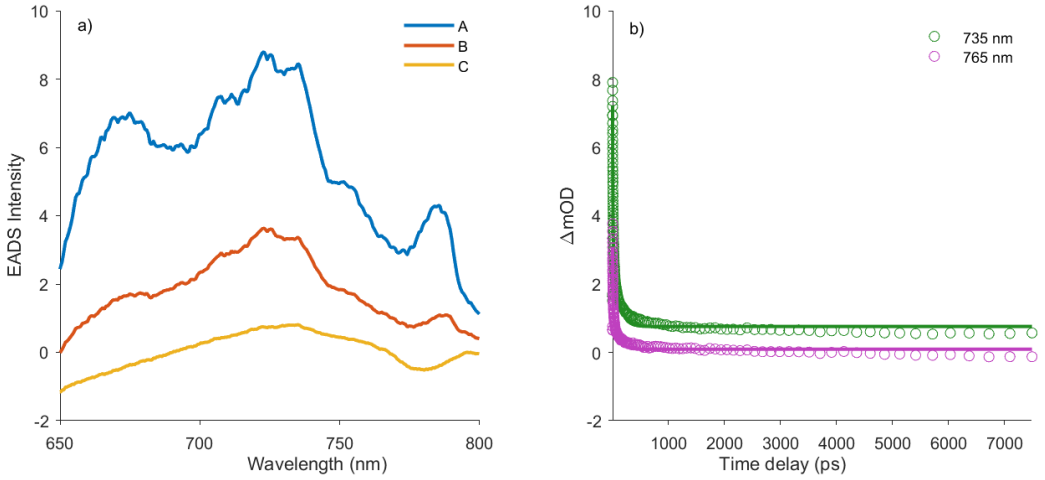

Figure 28: a) Evolution associated difference spectra corresponding to species A (blue), B (orange) and C (yellow). b) Kinetic traces at ~735 and 765 nm from 1 to 7500 ps, post excitation. Circles represent experimental data and solid lines represent fits obtained from global fitting.

Table 1 summarizes the time constants obtained for the three donor:PDI systems by fitting to a two-step sequential model (Equation 8). Even though these systems have the same electron acceptor molecules, the differences in the rate constants indicate that the charge carriers behave very differently from one system to another. To understand the mechanisms associated with each rate constant, theory calculations are required to identify the electronic states that may participate in the dynamics.

Table 1: k_1 and k_2 time constants obtained for different co-crystals by fitting a two-step sequential model

Co-crystal	$1/k_1$ (ps)	$1/k_2$ (ps)
PDI:PXX	279.86	1393.66
PDI:perylene	31.84	411.45
PDI:triphenylene	5.55	97.74

While Figure 28b shows that the experimental data is in good agreement with the sequential model, we cannot disregard the contribution of transport properties and EEA commonly seen in the exciton dynamics of organic D-A co-crystals. In addition to the excited states undergoing relaxation processes such as internal conversion, vibrational relaxation and ISC, the excited excitons can also travel from one D-A site to another. This allows the excited charge carriers to undergo processes such as EEA and exciton hopping. EEA is one such process that has been widely seen in similar organic co-crystals.[10, 11, 50]

The ESA feature in the PDI:triphenylene co-crystal can also be described by the kinetic model shown in Equation 9:

$$[A] \xrightarrow{k_1+k_2} [B] \xrightarrow{1/\infty} \quad (9)$$

where k_1 and k_2 are first- and second-order rate constants. A is the initial excited species and B is the non-decaying species that the system transforms to within the experimental time window. As given

in Equation 5, the k_1 rate constant represents the single exciton recombination pathway and k_2 represents EEA. Figure 29b shows kinetic traces obtained at different wavelengths to assess the goodness of the fit. The rate constants for k_1 and k_2 are $2.40*10^{-11}$ ps^{-1} and 0.11 ps^{-1} ΔmOD^{-1}, respectively. The EEA process dominates at early time delays when the exciton density is higher; as the exciton population decreases at longer time delays, single exciton recombination tends to dominate.

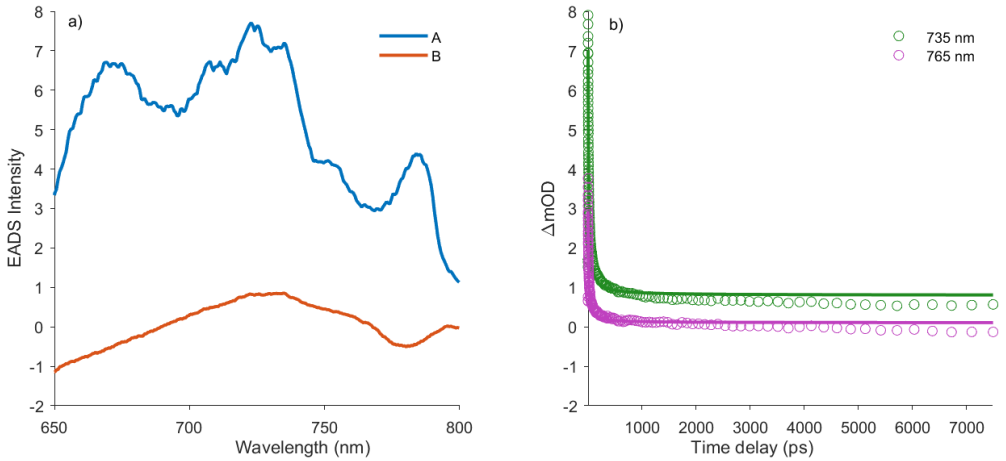

Figure 29: a) Evolution associated difference spectra corresponding to species A (blue) and B (orange). b) Kinetic traces at ~735 (green) and ~765 (purple) nm from 1 to 7500 ps post-excitation. Circles represent experimental data and solid lines represent fits obtained from global fitting.

For simplicity, we used the two models to describe electronic relaxation and exciton transport dynamics of the co-crystals, separately. It is important to note that electronic relaxation and exciton transport occur concurrently and factors such as crystallinity of the sample, pump fluence, and laser polarization will determine the dominant mechanism. [10, 11, 51]

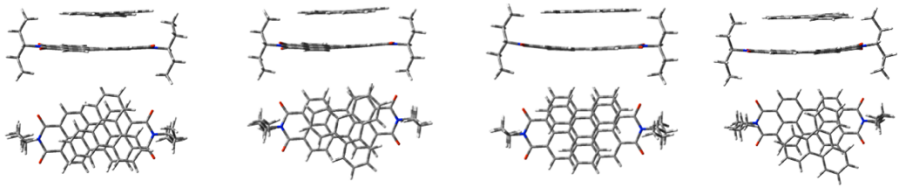

	3a	3b	3c	CIF
$Energy_{rel}$ (eV)	**0.000**	**0.003**	**0.033**	
DCT in S_1 (e)	**0.056**	**0.040**	**0.159**	
Osc. St. (au) of S_1	**0.628**	**0.639**	**0.595**	
DCT in S_2 (e)	**0.971**	**0.964**	**0.853**	
Osc. St. (au) of S_2	**0.011**	**0.013**	**0.057**	
DCT in S_0 (e)	**0.006**	**0.006**	**0.010**	

Figure 30: Optimized geometries (3a–c) of PDI:triphenylene computed with CAM-B3LYP-D3/6-31+G(d,p) and the experimental crystal structure. Energies (eV) are reported relative to the lowest-energy structure (3a) and include zero-point energy corrections. The calculated DCT is reported for S_0, S_1, and S_2 as well as their associated S_0–S_{1-2} oscillator strengths.

The PDI:triphenylene dimer PES was explored and different low-lying conformers were identified and compared to the experimental crystal structure, as shown in Figure 30. Like the other PDI:donor dimer systems, the relative energies of these conformers are very close. Interestingly, the DCT of the S_1 state is small like that of the ground state (S_0). In this system, the S_2 state is shown to be the CT state, with a DCT value close to 1e. We assessed differences between density functionals on the ordering of the CT states and found that the PBE functional[52] gave a S_1 CT state.

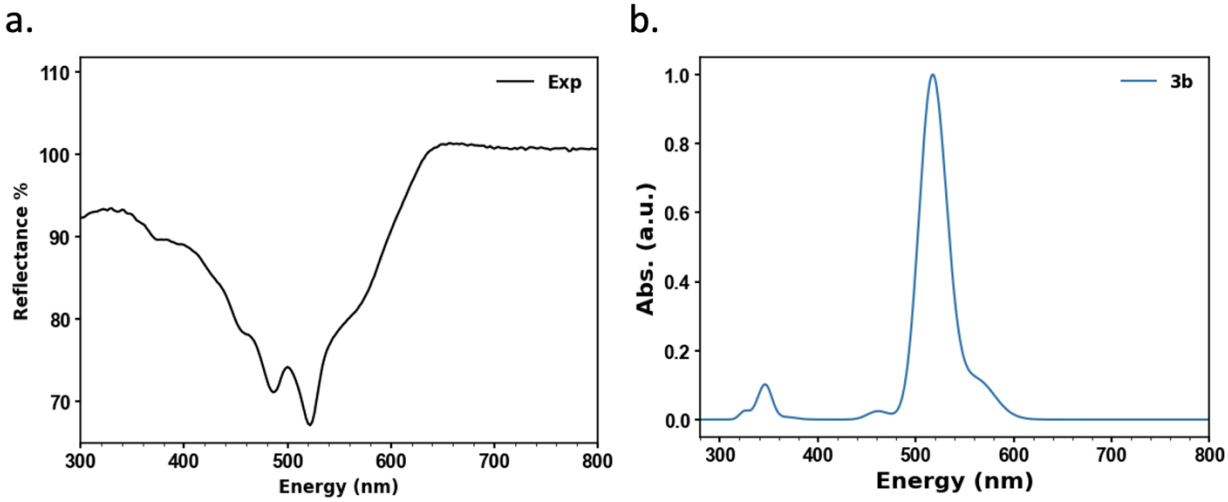

Figure 31: a) Diffuse reflectance spectra of PDI:triphenylene. b) The simulated absorption spectra of the best candidate dimer (Conformer 3b).

Using the PBE functional, we computed the UV-Vis spectra for the PDI:triphenylene conformers, finding that Conformer 3b resembled both the crystal structure and has the most similar UV-Vis spectrum, shown in Figure 31. The shoulder around 560 nm represents the S_1 CT state, in agreement with the other two PDI:donor systems. AIMD calculations to aid in assignment of the TAS are underway.

5. ASSESSING METRICS FOR COMPUTING DCT

5.1. Background

High-throughput screening (HTS) has become an essential tool in materials discovery. HTS is an automated, data-driven identification of promising candidate materials such as D-A co-crystals with a desired set of properties.[53] HTS tools search the vastness of chemical space to accelerate materials discovery, reducing experimental time and chemical waste. These tools often screen databases of crystal structures, spectroscopy, and quantum chemistry calculations, commonly supplementing these databases with on-the-fly quantum chemistry calculations.[54-58] For screening D-A co-crystals, quantum chemistry calculations include quantities such as geometric parameters, orbital energies, and vibrational frequencies.[59-62] In this project, we developed a new metric for screening D-A co-crystals with long exciton lifetimes, DCT in the S_1 state.[44, 63]

Computing the excited state properties of D-A co-crystals is primarily done with TDDFT. Unfortunately, many functionals have limitations in characterizing CT states; for more details, see Refs. [64, 65] and citations within. There are numerous techniques for predicting the DCT in electronically excited states, including natural bond order (NBO) analysis,[66] differences in orbital energies ($E_{HOMO}^{donor} - E_{LUMO}^{acceptor}$),[67] and the spatial overlap of the wavefunction, often referred to as the Λ metric.[46] Few systematic studies have been done to assess the quality of different metrics for computing DCT; a recent study from Herbert et al. highlights the importance of orbital invariance on qualitatively and quantitatively computing DCT. In this section we compare the performance of different DCT metrics, including the one developed in this project by McCaslin et al., for different functionals and basis sets.[44]

In our previous paper we screened 29 D-A dimers whose S_1 states are dominated by a HOMO → LUMO transitions.[44] The donor molecules exhibit a diversity of molecular structures, while the acceptor molecules consist of 7,7,8,8-tetracyanoquinodimethane (TCNQ) and its fluorinated derivatives, FxTCNQ. By comparing the performance of these metrics with different DFT functionals and basis sets, our study aims to unveil the robustness, reliability, and limitations of these metrics for quantifying DCT in D-A complexes.

5.2. Assessing the quality of CT metrics

5.2.1. Dependence on density functional

In Figure 32 we assess the correlation between DCT of the S_1 state and four metrics—orbital similarity,[44] spatial overlap,[46] orbital gap ratio,[67] and E_{HOMO} - E_{LUMO}—employing five DFT functionals: CAM-B3LYP-D, M062X, ωB97X-D, PBE1PBE-D, and APFD using a 6-31G+(d,p) basis set. For the orbital similarity and spatial overlap metrics, all five DFT functionals demonstrate relatively high R^2 values, indicating strong linear correlation of these metrics with S_1 DCT. This uniformity across different functionals indicates that these metrics are largely insensitive to the choice of DFT functional. The orbital gap ratio and E_{HOMO} - E_{LUMO} metrics deviate significantly from linear behavior, indicating their sensitivity to the choice of DFT functional. The correlations employing the latter two functionals, PBE1PBE-D and APFD, exhibit lower R^2 values for all metrics, suggesting that CT states are not well represented by these functionals.

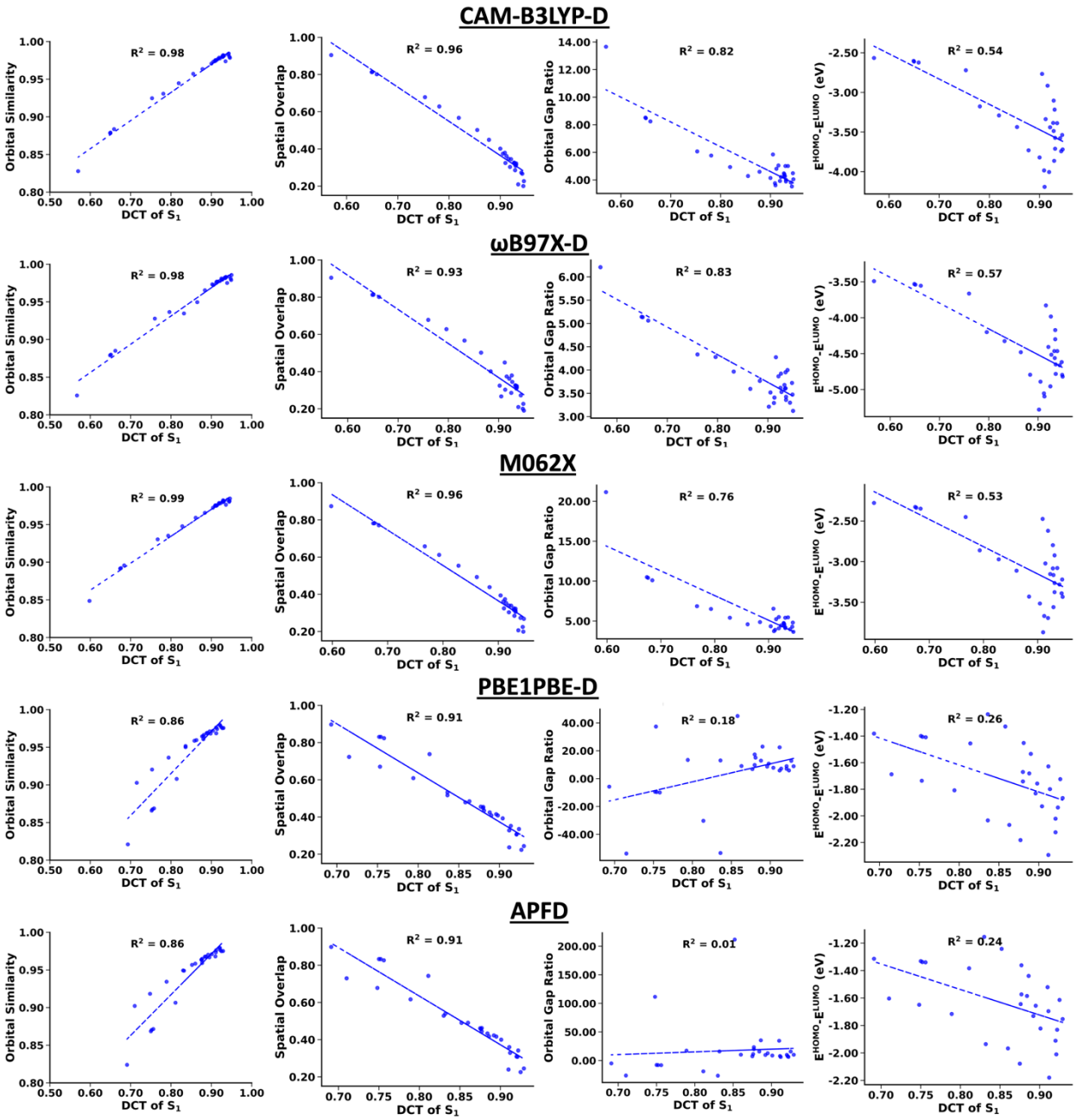

Figure 32: Plots of orbital similarity, spatial overlap, orbital gap ratio, and E_{HOMO} - E_{LUMO} vs. S_1 DCT using the CAM-B3LYP-D, ωB97X-D, M062X, PBE1PBE-D, and APFD functionals and a 6-31G+(d,p) basis set.

We summed the results of the five functionals into one plot, Figure 33, to assess overall correlation of these metrics with the DCT of S_1. The orbital similarity and spatial overlap metrics exhibit the strongest correlations with the DCT in the S_1 state, as indicated by their high R^2 values of 0.90 and 0.91, respectively. The value of the spatial overlap metric is inversely correlated to the S_1 DCT. Higher degrees of CT correspond to reduced spatial overlap between donor and acceptor orbitals in a D-A dimer. The insensitivity of both the orbital similarity and spatial overlap metrics to the DFT

functional choice is advantageous for performing quantum chemistry calculations, including those in HTS. In contrast, the orbital gap ratio and E_{HOMO} - E_{LUMO} metrics are not strongly correlated with S_1 DCT in this data set and exhibit significant sensitivity to functional.

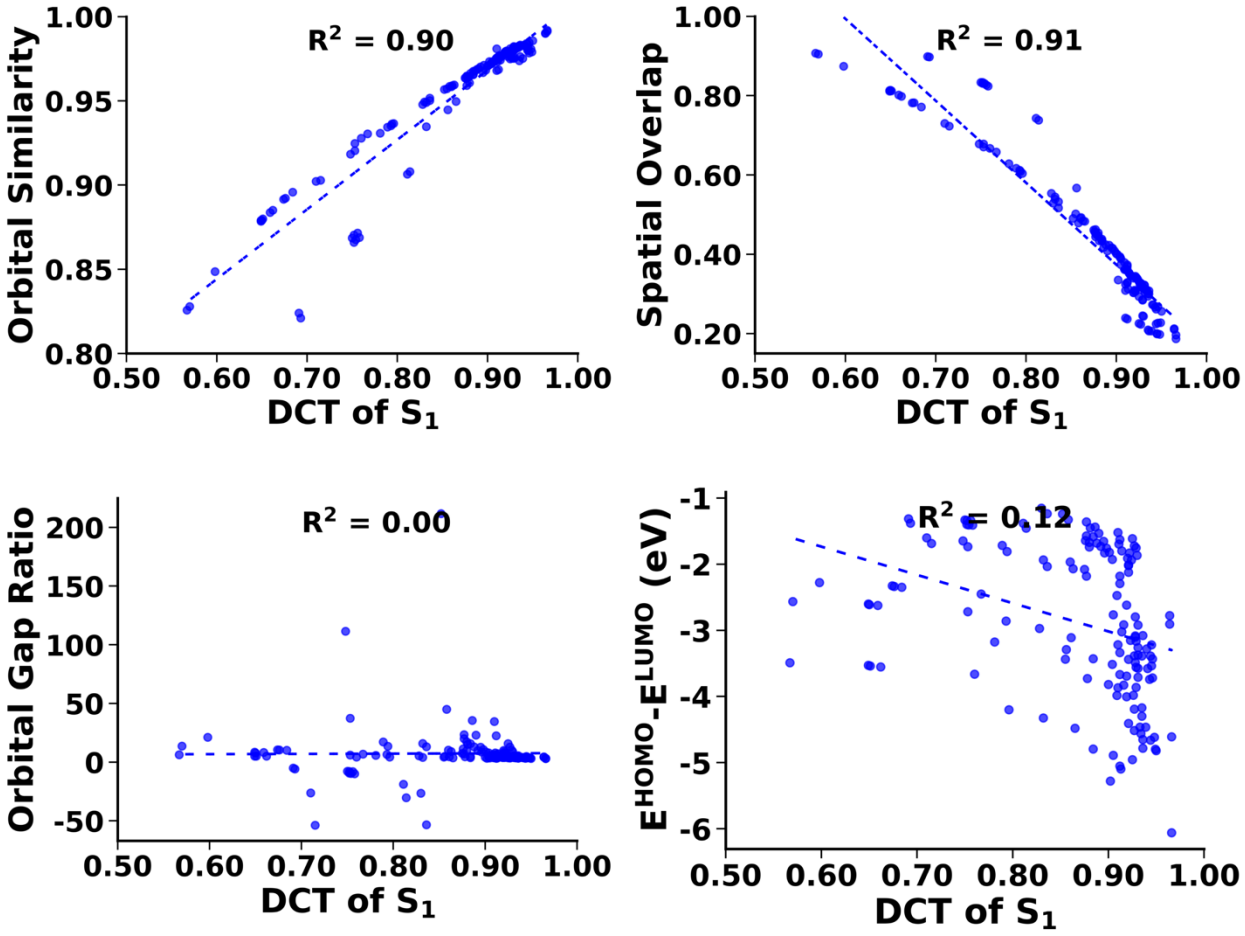

Figure 33: Plots of orbital similarity, spatial overlap, orbital gap ratio, and $E_{HOMO} - E_{LUMO}$ vs. S_1 DCT using the aggregated data across the five DFT functionals.

5.2.2. Dependence on basis set

To investigate the effect of the basis sets on these CT metrics, we selected the ωB97X-D functional to combine with three basis sets: 6-31G, 6-31+G(d,p), and 6-311++G(3df,3pd). The results in Figure 34 show that the orbital similarity metric is consistent in exhibiting strong linear correlation across all three basis sets with high R^2 values of 0.97, 0.98, and 0.98. Although the spatial overlap metric exhibits strong linear correlations with S_1 DCT, it exhibits slightly lower R^2 values ranging from 0.93 to 0.97. The orbital gap ratio and $E_{HOMO} - E_{LUMO}$ metrics exhibit a lower degree of

correlation overall and indicate sensitivity to basis set.

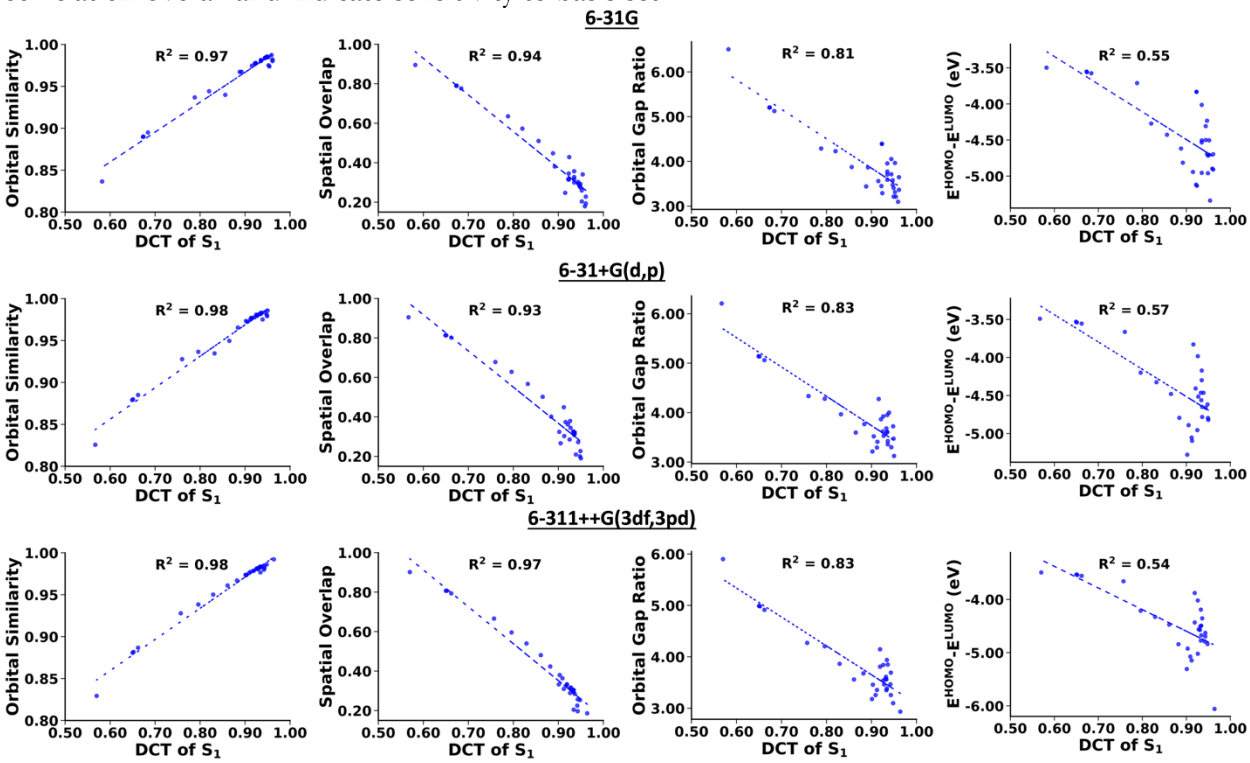

Figure 34: Plots of orbital similarity, spatial overlap, orbital gap ratio, and $E_{HOMO} - E_{LUMO}$ vs. S_1 DCT using ωB97X-D with 6-31G, 6-31+G(d,p), and 6-311++G(3df,3pd) basis sets.

6. PROFESSIONAL SERVICE

Our team engaged with the scientific community through a variety of modes. In addition to the standard ones such as publications and conference presentations, we served as reviewers for manuscripts submitted to peer-reviewed journals. In addition to fulfilling an essential professional service role, these activities raised the visibility of our team with influential stakeholders such as journal editors. Publications we reviewed for included many with direct relevance to this project, such as *ACS Applied Polymer Materials*, *Journal of the American Chemical Society*, *Advanced Materials*, *Chemical Science*, *Nature Energy*, *Journal of Physical Chemistry*, and *Physical Chemistry Chemical Physics*.

A tangible benefit afforded by these activities was an invitation to write a "News and Views" article for the journal *Nature Synthesis*. This invitation was extended by the journal's editor after Mark Allendorf reviewed a manuscript submitted to that journal.[68] The article describes a method for growing atomically smooth films of conducting materials that could be extended to the donor-acceptor materials we developed. In Allendorf's view the manuscript would likely have a high impact on the integration of novel conducting materials to create electro-optical devices and thus merited publication in this prestigious journal. The *News and Views* article is entitled "Skating on Thin Gallium" and was published in *Nature Synthesis* in 2024.[69]

REFERENCES

(1) Goetz, K. P.; Vermeulen, D.; Payne, M. E.; Kloc, C.; McNeil, L. E.; Jurchescu, O. D. Charge-transfer complexes: new perspectives on an old class of compounds. *Journal of Materials Chemistry C* **2014**, *2* (17), 3065-3076. DOI: 10.1039/C3TC32062F.

(2) Horiuchi, S.; Ishii, F.; Kumai, R.; Okimoto, Y.; Tachibana, H.; Nagaosa, N.; Tokura, Y. Ferroelectricity near room temperature in co-crystals of nonpolar organic molecules. *Nature Materials* **2005**, *4* (2), 163-166. DOI: 10.1038/nmat1298.

(3) Sun, L.; Wang, Y.; Yang, F.; Zhang, X.; Hu, W. Cocrystal Engineering: A Collaborative Strategy toward Functional Materials. *Advanced Materials* **2019**, *31* (39), 1902328. DOI: 10.1002/adma.201902328.

(4) Li, C.; Liu, M.; Pschirer, N. G.; Baumgarten, M.; Müllen, K. Polyphenylene-Based Materials for Organic Photovoltaics. *Chemical Reviews* **2010**, *110* (11), 6817-6855. DOI: 10.1021/cr100052z.

(5) Majumdar, P.; Tharammal, F.; Gierschner, J.; Varghese, S. Tuning Solid-State Luminescence in Conjugated Organic Materials: Control of Excitonic and Excimeric Contributions through π Stacking and Halogen Bond Driven Self-Assembly. *ChemPhysChem* **2020**, *21* (7), 616-624. DOI: 10.1002/cphc.201901223.

(6) Haarer, D.; Karl, N. Charge-transfer-absorption, CT-emission- and ESR-spectroscopy with zone-refined crystals of anthracene-pyromellitic dianhydride. *Chemical Physics Letters* **1973**, *21* (1), 49-53. DOI: 10.1016/0009-2614(73)80011-9.

(7) Haarer, D.; Philpott, M. R.; Morawitz, H. Field induced charge-transfer exciton transitions. *The Journal of Chemical Physics* **1975**, *63* (12), 5238-5245. DOI: 10.1063/1.431310.

(8) Haarer, D. Zero-phonon lines in the singlet spectrum of the charge transfer crystal anthracene-PMDA: Experimental evidence and model calculations. *The Journal of Chemical Physics* **1977**, *67* (9), 4076-4085. DOI: 10.1063/1.435383.

(9) Wang, C.; Malinoski, A. Perspective: Mechanistic investigations of photocatalytic processes with time-resolved optical spectroscopy. *The Journal of Chemical Physics* **2022**, *157* (16), 160901. DOI: 10.1063/5.0111162.

(10) Myong, M. S.; Qi, Y.; Stern, C.; Wasielewski, M. R. Ultrafast photo-driven charge transfer exciton dynamics in mixed-stack pyrene-perylenediimide single co-crystals. *Journal of Materials Chemistry C* **2021**, *9* (47), 16911-16917. DOI: 10.1039/D1TC04313G.

(11) Schlesinger, I.; Powers-Riggs, N. E.; Logsdon, J. L.; Qi, Y.; Miller, S. A.; Tempelaar, R.; Young, R. M.; Wasielewski, M. R. Charge-transfer biexciton annihilation in a donor–acceptor co-crystal yields high-energy long-lived charge carriers. *Chemical Science* **2020**, *11* (35), 9532-9541. DOI: 10.1039/D0SC03301D.

(12) Ding, Y.; Zhao, Y.; Liu, Y. Organic cocrystals: From high-performance molecular materials to multi-functional applications. *Aggregate* **2024**, e626. DOI: 10.1002/agt2.626.

(13) Sun, L.; Zhu, W.; Zhang, X.; Li, L.; Dong, H.; Hu, W. Creating Organic Functional Materials beyond Chemical Bond Synthesis by Organic Cocrystal Engineering. *Journal of the American Chemical Society* **2021**, *143* (46), 19243-19256. DOI: 10.1021/jacs.1c07678.

(14) Jiang, M.; Zhen, C.; Li, S.; Zhang, X.; Hu, W. Organic Cocrystals: Recent Advances and Perspectives for Electronic and Magnetic Applications. *Frontiers in Chemistry* **2021**, *9*. DOI: 10.3389/fchem.2021.764628.

(15) Leong, K.; Foster, M. E.; Wong, B. M.; Spoerke, E. D.; Van Gough, D.; Deaton, J. C.; Allendorf, M. D. Energy and charge transfer by donor–acceptor pairs confined in a metal–organic framework: a spectroscopic and computational investigation. *Journal of Materials Chemistry A* **2014**, *2* (10), 3389-3398. DOI: 10.1039/C3TA14328G.

(16) Müller, C.; Pascher, T.; Eriksson, A.; Chabera, P.; Uhlig, J. KiMoPack: A python Package for Kinetic Modeling of the Chemical Mechanism. *The Journal of Physical Chemistry A* **2022**, *126* (25), 4087-4099. DOI: 10.1021/acs.jpca.2c00907.
(17) Pensack, R. D.; Ostroumov, E. E.; Tilley, A. J.; Mazza, S.; Grieco, C.; Thorley, K. J.; Asbury, J. B.; Seferos, D. S.; Anthony, J. E.; Scholes, G. D. Observation of Two Triplet-Pair Intermediates in Singlet Exciton Fission. *The Journal of Physical Chemistry Letters* **2016**, *7* (13), 2370-2375. DOI: 10.1021/acs.jpclett.6b00947.
(18) Yanai, T.; Tew, D. P.; Handy, N. C. A new hybrid exchange–correlation functional using the Coulomb-attenuating method (CAM-B3LYP). *Chemical Physics Letters* **2004**, *393* (1), 51-57. DOI: 10.1016/j.cplett.2004.06.011.
(19) Hariharan, P. C.; Pople, J. A. The influence of polarization functions on molecular orbital hydrogenation energies. *Theoretica chimica acta* **1973**, *28*, 213-222. DOI: 10.1007/BF00533485.
(20) Hehre, W. J.; Ditchfield, R.; Pople, J. A. Self—Consistent Molecular Orbital Methods. XII. Further Extensions of Gaussian—Type Basis Sets for Use in Molecular Orbital Studies of Organic Molecules. *The Journal of Chemical Physics* **1972**, *56* (5), 2257-2261. DOI: 10.1063/1.1677527.
(21) Grimme, S.; Ehrlich, S.; Goerigk, L. Effect of the damping function in dispersion corrected density functional theory. *Journal of Computational Chemistry* **2011**, *32* (7), 1456-1465. DOI: 10.1002/jcc.21759.
(22) Bauernschmitt, R.; Ahlrichs, R. Treatment of electronic excitations within the adiabatic approximation of time dependent density functional theory. *Chemical Physics Letters* **1996**, *256* (4), 454-464. DOI: 10.1016/0009-2614(96)00440-X.
(23) Casida, M. E.; Jamorski, C.; Casida, K. C.; Salahub, D. R. Molecular excitation energies to high-lying bound states from time-dependent density-functional response theory: Characterization and correction of the time-dependent local density approximation ionization threshold. *The Journal of Chemical Physics* **1998**, *108* (11), 4439-4449. DOI: 10.1063/1.475855.
(24) Stratmann, R. E.; Scuseria, G. E.; Frisch, M. J. An efficient implementation of time-dependent density-functional theory for the calculation of excitation energies of large molecules. *The Journal of Chemical Physics* **1998**, *109* (19), 8218-8224. DOI: 10.1063/1.477483.
(25) Gaussian 16, Revision C.01, Frisch, M. J.; Trucks, G. W.; Schlegel, H. B.; Scuseria, G. E.; Robb, M. A.; Cheeseman, J. R.; Scalmani, G.; Barone, V.; Petersson, G. A.; Nakatsuji, H.; Li, X.; Caricato, M.; Marenich, A. V.; Bloino, J.; Janesko, B. G.; Gomperts, R.; Mennucci, B.; Hratchian, H. P.; Ortiz, J. V.; Izmaylov, A. F.; Sonnenberg, J. L.; Williams-Young, D.; Ding, F.; Lipparini, F.; Egidi, F.; Goings, J.; Peng, B.; Petrone, A.; Henderson, T.; Ranasinghe, D.; Zakrzewski, V. G.; Gao, J.; Rega, N.; Zheng, G.; Liang, W.; Hada, M.; Ehara, M.; Toyota, K.; Fukuda, R.; Hasegawa, J.; Ishida, M.; Nakajima, T.; Honda, Y.; Kitao, O.; Nakai, H.; Vreven, T.; Throssell, K.; Montgomery, J. A., Jr.; Peralta, J. E.; Ogliaro, F.; Bearpark, M. J.; Heyd, J. J.; Brothers, E. N.; Kudin, K. N.; Staroverov, V. N.; Keith, T. A.; Kobayashi, R.; Normand, J.; Raghavachari, K.; Rendell, A. P.; Burant, J. C.; Iyengar, S. S.; Tomasi, J.; Cossi, M.; Millam, J. M.; Klene, M.; Adamo, C.; Cammi, R.; Ochterski, J. W.; Martin, R. L.; Morokuma, K.; Farkas, O.; Foresman, J. B.; Fox, D. J. Gaussian, Inc., Wallingford CT, 2016.
(26) Tully, J. C. Molecular dynamics with electronic transitions. *The Journal of Chemical Physics* **1990**, *93* (2), 1061-1071. DOI: 10.1063/1.459170.
(27) Barbatti, M.; Bondanza, M.; Crespo-Otero, R.; Demoulin, B.; Dral, P. O.; Granucci, G.; Kossoski, F.; Lischka, H.; Mennucci, B.; Mukherjee, S.; et al. Newton-X Platform: New Software Developments for Surface Hopping and Nuclear Ensembles. *Journal of Chemical Theory and Computation* **2022**, *18* (11), 6851-6865. DOI: 10.1021/acs.jctc.2c00804.

(28) Hillery, M.; O'Connell, R. F.; Scully, M. O.; Wigner, E. P. Distribution functions in physics: Fundamentals. *Physics Reports* **1984**, *106* (3), 121-167. DOI: 10.1016/0370-1573(84)90160-1.
(29) Gilbert, A. T. B.; Besley, N. A.; Gill, P. M. W. Self-Consistent Field Calculations of Excited States Using the Maximum Overlap Method (MOM). *The Journal of Physical Chemistry A* **2008**, *112* (50), 13164-13171. DOI: 10.1021/jp801738f.
(30) Barca, G. M. J.; Gilbert, A. T. B.; Gill, P. M. W. Simple Models for Difficult Electronic Excitations. *Journal of Chemical Theory and Computation* **2018**, *14* (3), 1501-1509. DOI: 10.1021/acs.jctc.7b00994.
(31) Shao, Y.; Gan, Z.; Epifanovsky, E.; Gilbert, A. T. B.; Wormit, M.; Kussmann, J.; Lange, A. W.; Behn, A.; Deng, J.; Feng, X.; et al. Advances in molecular quantum chemistry contained in the Q-Chem 4 program package. *Molecular Physics* **2015**, *113* (2), 184-215. DOI: 10.1080/00268976.2014.952696.
(32) Marenich, A. V.; Cramer, C. J.; Truhlar, D. G. Universal Solvation Model Based on Solute Electron Density and on a Continuum Model of the Solvent Defined by the Bulk Dielectric Constant and Atomic Surface Tensions. *The Journal of Physical Chemistry B* **2009**, *113* (18), 6378-6396. DOI: 10.1021/jp810292n.
(33) Epifanovsky, E.; Gilbert, A. T. B.; Feng, X.; Lee, J.; Mao, Y.; Mardirossian, N.; Pokhilko, P.; White, A. F.; Coons, M. P.; Dempwolff, A. L.; et al. Software for the frontiers of quantum chemistry: An overview of developments in the Q-Chem 5 package. *The Journal of Chemical Physics* **2021**, *155* (8), 084801. DOI: 10.1063/5.0055522.
(34) Chai, J.-D.; Head-Gordon, M. Long-range corrected hybrid density functionals with damped atom–atom dispersion corrections. *Physical Chemistry Chemical Physics* **2008**, *10* (44), 6615-6620. DOI: 10.1039/B810189B.
(35) Austin, A.; Petersson, G. A.; Frisch, M. J.; Dobek, F. J.; Scalmani, G.; Throssell, K. A Density Functional with Spherical Atom Dispersion Terms. *Journal of Chemical Theory and Computation* **2012**, *8* (12), 4989-5007. DOI: 10.1021/ct300778e.
(36) Adamo, C.; Barone, V. Toward reliable density functional methods without adjustable parameters: The PBE0 model. *The Journal of Chemical Physics* **1999**, *110* (13), 6158-6170. DOI: 10.1063/1.478522.
(37) Ernzerhof, M.; Scuseria, G. E. Assessment of the Perdew–Burke–Ernzerhof exchange-correlation functional. *The Journal of Chemical Physics* **1999**, *110* (11), 5029-5036. DOI: 10.1063/1.478401.
(38) Zhao, Y.; Truhlar, D. G. The M06 suite of density functionals for main group thermochemistry, thermochemical kinetics, noncovalent interactions, excited states, and transition elements: two new functionals and systematic testing of four M06-class functionals and 12 other functionals. *Theoretical Chemistry Accounts* **2008**, *120* (1), 215-241. DOI: 10.1007/s00214-007-0310-x.
(39) Grimme, S.; Hansen, A.; Brandenburg, J. G.; Bannwarth, C. Dispersion-Corrected Mean-Field Electronic Structure Methods. *Chemical Reviews* **2016**, *116* (9), 5105-5154. DOI: 10.1021/acs.chemrev.5b00533.
(40) Ditchfield, R.; Hehre, W. J.; Pople, J. A. Self-Consistent Molecular-Orbital Methods. IX. An Extended Gaussian-Type Basis for Molecular-Orbital Studies of Organic Molecules. *The Journal of Chemical Physics* **1971**, *54* (2), 724-728. DOI: 10.1063/1.1674902.
(41) Clark, T.; Chandrasekhar, J.; Spitznagel, G. W.; Schleyer, P. V. R. Efficient diffuse function-augmented basis sets for anion calculations. III. The 3-21+G basis set for first-row elements, Li–F. *Journal of Computational Chemistry* **1983**, *4* (3), 294-301. DOI: 10.1002/jcc.540040303.

(42) Frisch, M. J.; Pople, J. A.; Binkley, J. S. Self-consistent molecular orbital methods 25. Supplementary functions for Gaussian basis sets. *The Journal of Chemical Physics* **1984**, *80* (7), 3265-3269. DOI: 10.1063/1.447079.
(43) Krishnan, R.; Binkley, J. S.; Seeger, R.; Pople, J. A. Self-consistent molecular orbital methods. XX. A basis set for correlated wave functions. *The Journal of Chemical Physics* **1980**, *72* (1), 650-654. DOI: 10.1063/1.438955.
(44) Abou Taka, A.; Herbert, J. M.; McCaslin, L. M. Ground-State Orbital Analysis Predicts S1 Charge Transfer in Donor–Acceptor Materials. *The Journal of Physical Chemistry Letters* **2023**, *14* (49), 11063-11068. DOI: 10.1021/acs.jpclett.3c02787.
(45) Plasser, F. TheoDORE: A toolbox for a detailed and automated analysis of electronic excited state computations. *The Journal of Chemical Physics* **2020**, *152* (8), 084108. DOI: 10.1063/1.5143076.
(46) Peach, M. J. G.; Benfield, P.; Helgaker, T.; Tozer, D. J. Excitation energies in density functional theory: An evaluation and a diagnostic test. *The Journal of Chemical Physics* **2008**, *128* (4), 044118. DOI: 10.1063/1.2831900.
(47) Lu, T.; Chen, F. Multiwfn: A multifunctional wavefunction analyzer. *Journal of Computational Chemistry* **2012**, *33* (5), 580-592. DOI: 10.1002/jcc.22885.
(48) Zhao, Y.; Wang, V.; Javey, A. Molecular Materials with Short Radiative Lifetime for High-Speed Light-Emitting Devices. *Matter* **2020**, *3* (6), 1832-1844. DOI: 10.1016/j.matt.2020.09.009.
(49) Williams, M. L.; Schlesinger, I.; Jacobberger, R. M.; Wasielewski, M. R. Mechanism of Ultrafast Triplet Exciton Formation in Single Cocrystals of π-Stacked Electron Donors and Acceptors. *Journal of the American Chemical Society* **2022**, *144* (40), 18607-18618. DOI: 10.1021/jacs.2c08584.
(50) Wang, K.; Chen, H.; Zhang, J.; Zou, Y.; Yang, Y. Intrachain and Interchain Exciton–Exciton Annihilation in Donor–Acceptor Copolymers. *The Journal of Physical Chemistry Letters* **2021**, *12* (16), 3928-3933. DOI: 10.1021/acs.jpclett.1c00369.
(51) Zheng, Y.; Venkatesh, R.; Rojas-Gatjens, E.; Reichmanis, E.; Silva-Acuña, C. Exciton Bimolecular Annihilation Dynamics in Push–Pull Semiconductor Polymers. *The Journal of Physical Chemistry Letters* **2024**, *15* (1), 272-280. DOI: 10.1021/acs.jpclett.3c03094.
(52) Perdew, J. P.; Burke, K.; Ernzerhof, M. Generalized Gradient Approximation Made Simple. *Physical Review Letters* **1996**, *77* (18), 3865-3868. DOI: 10.1103/PhysRevLett.77.3865.
(53) Curtarolo, S.; Hart, G. L. W.; Nardelli, M. B.; Mingo, N.; Sanvito, S.; Levy, O. The high-throughput highway to computational materials design. *Nature Materials* **2013**, *12* (3), 191-201. DOI: 10.1038/nmat3568.
(54) Wu, Y.; Guo, J.; Sun, R.; Min, J. Machine learning for accelerating the discovery of high-performance donor/acceptor pairs in non-fullerene organic solar cells. *npj Computational Materials* **2020**, *6* (1), 120. DOI: 10.1038/s41524-020-00388-2.
(55) Ju, C.-W.; Bai, H.; Li, B.; Liu, R. Machine Learning Enables Highly Accurate Predictions of Photophysical Properties of Organic Fluorescent Materials: Emission Wavelengths and Quantum Yields. *Journal of Chemical Information and Modeling* **2021**, *61* (3), 1053-1065. DOI: 10.1021/acs.jcim.0c01203.
(56) Mahmood, A.; Wang, J.-L. Machine learning for high performance organic solar cells: current scenario and future prospects. *Energy & Environmental Science* **2021**, *14* (1), 90-105. DOI: 10.1039/D0EE02838J.
(57) Rodríguez-Martínez, X.; Pascual-San-José, E.; Campoy-Quiles, M. Accelerating organic solar cell material's discovery: high-throughput screening and big data. *Energy & Environmental Science* **2021**, *14* (6), 3301-3322. DOI: 10.1039/D1EE00559F.

(58) Liu, X.; Shao, Y.; Lu, T.; Chang, D.; Li, M.; Lu, W. Accelerating the discovery of high-performance donor/acceptor pairs in photovoltaic materials via machine learning and density functional theory. *Materials & Design* **2022**, *216*, 110561. DOI: 10.1016/j.matdes.2022.110561.
(59) Zhu, L.; Kim, E.-G.; Yi, Y.; Brédas, J.-L. Charge Transfer in Molecular Complexes with 2,3,5,6-Tetrafluoro-7,7,8,8-tetracyanoquinodimethane (F4-TCNQ): A Density Functional Theory Study. *Chemistry of Materials* **2011**, *23* (23), 5149-5159. DOI: 10.1021/cm201798x.
(60) Behera, R. K.; Goud, N. R.; Matzger, A. J.; Brédas, J.-L.; Coropceanu, V. Electronic Properties of 1,5-Diaminonaphthalene:Tetrahalo-1,4-benzoquinone Donor–Acceptor Cocrystals. *The Journal of Physical Chemistry C* **2017**, *121* (42), 23633-23641. DOI: 10.1021/acs.jpcc.7b08360.
(61) Zhuo, M.-P.; Yuan, Y.; Su, Y.; Chen, S.; Chen, Y.-T.; Feng, Z.-Q.; Qu, Y.-K.; Li, M.-D.; Li, Y.; Hu, B.-W.; et al. Segregated Array Tailoring Charge-Transfer Degree of Organic Cocrystal for the Efficient Near-Infrared Emission beyond 760 nm. *Advanced Materials* **2022**, *34* (11), 2107169. DOI: 10.1002/adma.202107169.
(62) Shi, W.; Deng, T.; Wong, Z. M.; Wu, G.; Yang, S.-W. A molecular roadmap towards organic donor-acceptor complexes with high-performance thermoelectric response. *npj Computational Materials* **2021**, *7* (1), 107. DOI: 10.1038/s41524-021-00580-y.
(63) Abou Taka, A.; Reynolds, J. E.; Cole-Filipiak, N. C.; Shivanna, M.; Yu, C. J.; Feng, P.; Allendorf, M. D.; Ramasesha, K.; Stavila, V.; McCaslin, L. M. Comparing the structures and photophysical properties of two charge transfer co-crystals. *Physical Chemistry Chemical Physics* **2023**, *25* (40), 27065-27074. DOI: 10.1039/D3CP03720G.
(64) Herbert, J. M. Chapter 3 - Density-functional theory for electronic excited states. In *Theoretical and Computational Photochemistry*, García-Iriepa, C., Marazzi, M. Eds.; Elsevier, 2023; pp 69-118.
(65) Herbert, J. M.; Mandal, A. Importance of Orbital Invariance in Quantifying Electron-Hole Separation and Exciton Size. *ChemRxiv*. DOI: 10.26434/chemrxiv-2024-6dnh8
(66) Glendening, E. D.; Hiatt, D. M.; Weinhold, F. Natural Bond Orbital Analysis of Chemical Structure, Spectroscopy, and Reactivity: How it Works. In *Comprehensive Computational Chemistry (First Edition)*, Yáñez, M., Boyd, R. J. Eds.; Elsevier, 2024; pp 406-421.
(67) Blaskovits, J. T.; Fumanal, M.; Vela, S.; Corminboeuf, C. Designing Singlet Fission Candidates from Donor–Acceptor Copolymers. *Chemistry of Materials* **2020**, *32* (15), 6515-6524. DOI: 10.1021/acs.chemmater.0c01784.
(68) Liu, J.; Chen, Y.; Huang, X.; Ren, Y.; Hambsch, M.; Bodesheim, D.; Pohl, D.; Li, X.; Deconinck, M.; Zhang, B.; et al. On-liquid-gallium surface synthesis of ultrasmooth thin films of conductive metal–organic frameworks. *Nature Synthesis* **2024**, *3* (6), 715-726. DOI: 10.1038/s44160-024-00513-9.
(69) Allendorf, M. Skating on thin gallium. *Nature Synthesis* **2024**, *3* (6), 675-676. DOI: 10.1038/s44160-024-00532-6.

DISTRIBUTION

Email—Internal

Name	Org.	Sandia Email Address
Nils Hansen	8353	nhansen@sandia.gov
Craig Taatjes	8350	cataatj@sandia.gov
Sarah Allendorf	8300	swallen@sandia.gov
Jeff Tsao	1800	jytsao@sandia.gov
David Chandler	8300	chand@sandia.gov
Technical Library	1911	sanddocs@sandia.gov

Email—External

Name	Company Email Address	Company Name
Marissa Weichman	weichman@princeton.edu	Princeton University
John Herbert	herbert@chemistry.ohio-state.edu	Ohio State University

This page left blank

Sandia National Laboratories

Sandia National Laboratories is a multimission laboratory managed and operated by National Technology & Engineering Solutions of Sandia LLC, a wholly owned subsidiary of Honeywell International Inc. for the U.S. Department of Energy's National Nuclear Security Administration under contract DE-NA0003525.